Acta Materialia 237 (2022) 118156

Contents lists available at ScienceDirect

Acta Materialia

journal homepage: www.elsevier.com/locate/actamat

Precipitation-based grain boundary design alters Inter- to Trans-granular Fracture in AlCrN Thin Films

M. Meindlhumer[a,*], T. Ziegelwanger[b], J. Zalesak[c], M. Hans[d], L. Löfler[b,d], S. Spor[a,e], N. Jäger[a], A. Stark[f], H. Hruby[e], R. Daniel[a], D. Holec[b], J.M. Schneider[d], C. Mitterer[b], J. Keckes[b]

[a] Christian Doppler Laboratory for Advanced Synthesis of Novel Multifunctional Coatings at the Department of Materials Science, Montanuniversität Leoben, Leoben, Austria
[b] Department of Materials Science, Montanuniversität Leoben, Leoben, Austria
[c] Erich Schmid Institute for Materials Science, Austrian Academy of Sciences, Leoben, Austria
[d] Materials Chemistry, RWTH Aachen University, Aachen, Germany
[e] Voestalpine eifeler Vacotec GmbH, Düsseldorf, Germany
[f] Helmholtz-Zentrum Hereon, Geesthacht, Germany

ARTICLE INFO

Article history:
Received 28 February 2022
Revised 4 July 2022
Accepted 5 July 2022
Available online 6 July 2022

Keywords:
AlCrN
Heat treatment
Grain-boundary segregation engineering
Micromechanics

ABSTRACT

Despite their high hardness and indentation modulus, nanostructured crystalline ceramic thin films produced by physical vapour deposition usually lack sufficient fracture strength and toughness. This brittleness is often caused by underdense columnar grain boundaries of low cohesive energy, which serve as preferential paths for crack propagation. In this study, mechanical and structural properties of arc-evaporated $Al_{0.9}Cr_{0.1}N$ thin films were analyzed using micromechanical tests, electron microscopy, atom probe tomography and *in situ* high-energy high-temperature grazing incidence transmission X-ray diffraction. Vacuum annealing at 1100°C resulted in the formation of regularly-distributed globular cubic Cr(Al)N and elongated cubic CrN precipitates at intracrystalline Cr-enriched sublayers and at columnar grain boundaries with sizes of ~5 and ~30 nm, respectively. Consequently, *in situ* micromechanical testing before and after the heat treatment revealed simultaneous enhancement of Young's modulus, fracture stress and fracture toughness by ~35, 60 and 10%, respectively. The annealing-induced concomitant improvement of toughness and strength was inferred to precipitations observed within grains as well as at grain boundaries enhancing the cohesive energy of the grain boundaries and thereby altering the crack propagation pathway from inter- to transcrystalline. The here reported experimental data unveil the hitherto untapped potential of precipitation-based grain boundary design for the improvement of mechanical properties of transition metal nitride thin films.

1. Introduction

Though transition metal nitride (TMN) thin films are intrinsically hard, having beneficial high *Young's modulus E* and *hardness H*, intercolumnar cracking at grain boundaries of relatively low cohesive energy is typically observed, resulting in low *fracture stress* σ_F and *toughness* K_{IC} [1,2].

Several synthesis strategies have been used to alter the microstructure and the resulting K_{IC} of physical vapour-deposited (PVD) TMN thin films, such as (i) elemental alloying, which leads to the formation of metastable supersaturated solid solutions of higher intrinsic toughness [3,4], as well as extrinsic toughening achieved by (ii) application of multi-layers and superlattices with alternating mechanical properties along the cross-sectional crack path [5,6] and (iii) growth of sculptured films with tilted grain boundaries to increase the effective crack length [2]. For example, alloying of TiN with Al led to an increase of K_{IC} from 1.9 to ~2.7 MPa $m^{½}$ [4] and further addition of 15 at.% Ta could improve K_{IC} to ~4.7 MPa $m^{½}$ [3]. In the case of multi-layer films, a 60% increase of K_{IC} was reported for the TiN-SiO_x system, whereby the K_{IC} increase is even more pronounced for superlattice thin films, with K_{IC} values of up to 4.7 MPa $m^{½}$ reported for a TiN/WN superlattice with a bilayer period of 10.2 nm [7]. Additionally, sculpturing of TiN grains led to an increase of K_{IC} to 3.1 MPa $m^{½}$ [2], while implementing SiO_x between differently oriented TiN sublayers resulted in a further K_{IC} increase to 3.5 MPa $m^{½}$ [8].

* Corresponding author.
E-mail address: michael.meindlhumer@unileoben.ac.at (M. Meindlhumer).

https://doi.org/10.1016/j.actamat.2022.118156

Furthermore, in the case of technologically relevant TMNs, both high H and K_{IC} have to be combined with sufficient *thermal stability* of phases and microstructure as well as a *good oxidation* resistance up to ~1000°C. Limited experimental data is however available on the alteration of fracture properties of PVD thin films during or after annealing. In the case of CrN [9] and TiN [10], annealing above the deposition temperature caused a significant deterioration of fracture properties, which has been attributed to a defect annihilation at the grain boundaries [9,10], a compressive residual stress relaxation [11] and a pore formation at the grain boundaries [10]. In the case of Al-rich cubic (c) TiAlN [4], spinodal decomposition resulted in an increase of K_{IC} at ~850°C, whereas segregation of wurtzite (w) AlN at temperatures above 950°C caused a drop in H, E and K_{IC} [4]. Even before w-AlN had been segregated from CrAlN, a drop of K_{IC} from 2.5 to 1.5 MPa $m^{½}$ after annealing at 700°C was found by Drnovsek *et al.* [12]. Exemplary, for the case of single crystalline TiN/NbN superlattice thin films on MgO, the thermal stability was found to be limited to ~900°C with interdiffusion and alloying of the individual sublayers, which deteriorate mechanical properties [13,14]. That study did not consider the diffusion along grain boundaries, which is however of high importance for technologically relevant TMN films. Generally, it can be stated, that despite the above achievements in improving K_{IC} by alloying and microstructural design of as-deposited TMN thin films, when the films are exposed to high temperatures their mechanical properties deteriorate, due to the interdiffusion of alloying elements, decomposition of metastable supersaturated alloys and/or degradation of the multi-layered structures [4,13,14]. However, the authors are not aware of any published studies addressing the toughening of columnar grain boundaries of PVD thin films by using a dedicated grain boundary segregation. For w-ZrAlN PVD films, indeed, precipitation of c-ZrN at the columnar grain boundaries was reported after annealing to 1100°C, although no mechanical properties were investigated in that pioneering study [15].

Grain boundary segregation engineering [16] was exploited for several bulk metal alloys in the recent years, where the most scientific interest was drawn on martensitic steel with medium Mn content (8–12 wt.%). Grain boundary segregation engineering was performed by a 48 h long annealing treatment at 500°C in a Fe-12 wt.% Mn alloy, where a reverse transformation of lath martensite into austenite at the grain boundaries, accompanied by subsequent toughening was achieved. The annealing leads to a Mn excess on the grain boundary of up to 25%, thus stabilizing the ductile/tough austenite phase [17]. Another example is bulk Mo, which suffers from brittle intercrystalline failure, where a grain boundary segregation engineering has been used to (i) adjust the brittle-to-ductile-transition temperature below room temperature (RT) and (ii) to change fracture behavior from inter- to trans-granular [18–20].

As mentioned above, the available literature shows the limited thermal stability of mechanical properties of conventional ternary c-TiAlN and c-CrAlN thin films, with significant deterioration of mechanical properties at 950 [4] and 700°C [12,21], respectively. In contrast, $Al_xTi_{1-x}N$ films with Al contents of up to $x = 0.95$ and high Al-containing AlCrN films alloyed with Si led to the formation of predominantly *wurtzite crystal structure with superior thermal stability and oxidation resistance* [22–24]. However, no detailed analysis of the influence of microstructural changes on mechanical properties and their stability was given in these studies. Given the reported precipitation at 1100°C in w-ZrAlN [15], this work aims to highlight the possibilities of the w-$Al_{0.9}Cr_{0.1}N$ thin film system, which was up to now mostly neglected in literature.

Here, we present a comprehensive structural, compositional and micromechanical analysis of a nanocrystalline $Al_{0.9}Cr_{0.1}N$ thin film, which consisted of wurtzite B4 crystal structure in the as-deposited state. After being subjected to a heat treatment with a peak temperature of 1100°C, the film microstructure turned primarily to a composite of w-AlCrN columnar grains, with c-CrN and c-Cr(Al)N precipitates formed at grain boundaries and at former periodic Cr-enriched compositional modulations within the grains, respectively. Consequently, the fracture mode switched from intercolumnar (in the as-deposited state) to trans-columnar fracture (in the annealed state), while simultaneously enhancing E, σ_F and K_{IC}. The reported enhancement of mechanical properties demonstrates the enormous untapped potential of grain boundary design in the synthesis of hard and tough TMN thin films.

2. Methods

2.1. Thin film synthesis

The ~12.2 µm thick $Al_{0.9}Cr_{0.1}N$ (further denoted as w-AlCrN) thin film was prepared by cathodic arc evaporation in a voestalpine eifeler-Vacotec alpha400P deposition system equipped with six $Al_{0.9}Cr_{0.1}$ cathodes operated at a cathode current of 100 A, substrate bias voltage $U_B = -100$ V, nitrogen pressure $p_{N_2} = 4$ Pa and a substrate temperature of $T_S = 475$°C. The mirror-polished cemented carbide (WC, 10 wt.% Co) substrates of a dimension of $10 \times 5 \times 5$ mm³ were mounted on the sample holder in one-fold-rotation using a rotation speed of 2 rpm at a minimum cathode-to-substrate distance of ~100 mm and plasma cleaning was employed prior deposition.

2.2. In situ *high-temperature high-energy X-ray diffraction*

The *in situ* high-energy high-temperature grazing incidence transmission X-ray diffraction (HE-HT-GIT-XRD) [21] experiments were performed at the P07B beamline of the PETRA III synchrotron source in Hamburg (D) in transmission geometry, using a pencil X-ray beam with a size of 400 µm × 100 µm and an energy of 87.1 keV. The samples were mounted into a DIL 805 dilatometer (TA Instruments) with the surface aligned with respect to the primary beam at an incident angle β of ~2 deg.

The thermal cycle included heating to 1100°C at a rate of 1 K/s followed by a holding segment of 300 s at the maximum temperature (both in vacuum at $p_{total} < 10^{-2}$ mbar) and subsequent cooling to room temperature (RT) at a rate of ~1 K/s, controlled by the Ar flow through the dilatometer chamber. The heating and cooling rates were adjusted for receiving sufficient diffracted signal at the 2D detector, which can be revised together with further experimental details in Ref. [21].

2.3. Electron microscopy

Cross-sections from as-deposited and annealed $Al_{0.9}Cr_{0.1}N$ films were fabricated using a Zeiss CrossBeam 1540XB focused ion beam (FIB) microscope. First a tungsten protection layer was deposited using the gas injection system and polishing currents ranging from to 200 pA to 10 pA were used. Cross-sectional characterization was performed in a Zeiss LEO 1525 scanning electron microscope (SEM) with 3 kV accelerating voltage using an aperture of 20 µm. Additionally, fracture surfaces were characterised after the *in situ* cantilever bending experiments (*cf.* Section 2.5) applying the former parameter set at an inclination angle of 45 deg. Energy dispersive X-ray spectroscopy (EDS) was performed in SEM using built-in standards (Zeiss LEO 1525, Bruker Quantax, with 10 kV accelerating voltage and 60 µm aperture). Twenty EDS measurements were performed for as-deposited and annealed films quantifying Al, Cr, N, and O contents.

Electron beam-transparent cross-sectional lamellae for transmission electron microscopy (TEM) analyses were prepared by a FEI Helios NanoLab 660 FIB. The Ga^+-ion source was operated at

stepwise decreased accelerating voltages of 30, 5 and 2 kV and constantly decreasing ion currents of 40 nA to 50 pA. Scanning transmission electron microscopy (STEM) and EDS analysis were performed using a FEI Titan Themis operated at an acceleration voltage of 300 kV. The EDS analysis were performed using a four-quadrant detector and a probe current of 1 nA, while the recorded data were treated using the Velox software and quantified by built-in standards. Selected area electron diffraction (SAED) was performed using a JEOL 2200FS microscope operating at an acceleration voltage of 200 kV. An in-column omega filter was utilised to center a 5 eV wide aperture around a zero-loss peak to enhance the signal-to-noise ratio in the SAED micrograph. The diffraction data was processed and indexed in a CrysTBox software [25].

2.4. Atom probe tomography

The local chemical composition at the nanometre scale of the as-deposited and 1100°C annealed thin films was investigated by atom probe tomography (APT). Field evaporation was assisted by laser pulsing using a CAMECA local electrode atom probe 4000X HR. It has been demonstrated for a $(Ti_{0.255}Al_{0.235})(N_{0.505}O_{0.005})$ thin film that the absolute Al composition from APT is overestimated, while the N composition is underestimated [26]. Since the measurement accuracy is governed by the electric field strength, a relatively low laser pulse energy of 10 pJ was used in order to increase the ionization probability of neutral species [27]. The laser pulse frequency, base temperature and detection rate were set at 200 kHz, 60 K and 5 ions out of 1000 applied laser pulses, respectively. At least 20 million ions were detected and the IVAS 3.8.0 software was used for data analysis, employing the shank angle reconstruction protocol. Based on TEM data, the reconstruction parameters were tuned towards a bilayer thickness of 34 nm in case of the as-deposited thin film (*cf.* Fig. 5). Similar reconstruction parameters were adopted for the thin film annealed at 1100°C, taking the initial specimen geometry differences into account. Needle-shaped specimens were prepared by FIB according to a standard protocol [28] using a FEI Helios Nanolab 660 dual-beam microscope.

2.5. Micromechanical testing

Indentation modulus E_i and hardness H of the films in as-deposited and annealed state were determined by means of nanoindentation (UMIS, Fischer-Cripps Laboratory Ltd.). *In situ* micromechanical tests were carried out in a ZEISS LEO 982 SEM equipped with a Hysitron PI 85 nanoindenter. At first, cantilevers of $L \times B \times t \sim 12 \times 2 \times 2.9\,\mu m^3$ from the as-deposited and annealed $Al_{0.9}Cr_{0.1}N$ films were fabricated using a ZEISS LEO CrossBeam 1540XB workstation using a set of milling currents ranging from 5 nA for removal of the substrate down to 100 pA for final polishing. Special care was taken to avoid cantilever damage from Ga^+ ions by using low FIB milling currents at the final cantilever preparation steps in agreement with [29,30]. The samples were loaded and fractured using a sphero-conical indenter tip (Synton MDP AG, Switzerland) with a tip radius of 700 nm using a loading speed of 20 nm/s applied in a displacement-controlled feedback loop. The received load (P)-deflection (w) curves were corrected for instrument compliance. In addition to the indentation modulus derived from the nanoindentation experiments, the elastic modulus E was calculated from the slope $\frac{dP}{dw}$ of the load-deflection curves as follows

$$E = \frac{4}{B} \times \frac{dP}{dw} \times \left(\frac{L}{t}\right)^3, \tag{1}$$

where P and w are load and deflection of the cantilever during loading, B, L and t are the width, the length and the thickness of the cantilever, respectively. From the maximum applied load at fracture P_{max}, the fracture stress σ_F was calculated according to

$$\sigma_F = 6\frac{P_{max}L}{Bt^2}. \tag{2}$$

In order to determine the fracture toughness K_{IC} of the films, a notch with a depth of $a \sim 600$ nm was added at 2 µm distance from the ground using a current of 10 pA for 90 s on half of the cantilevers in agreement with the recommendations of Best *et al.* [30]. By applying linear elastic fracture mechanics, K_{IC} was calculated as

$$K_{IC} = \sigma_F\sqrt{\pi a} \times Y\left(\frac{a}{t}\right), \tag{3}$$

where $Y(\frac{a}{t})$ is the dimensionless shape factor derived by Ref. [31] for the freestanding cantilever geometry.

$$Y\left(\frac{a}{t}\right) = \sqrt{\frac{2t}{\pi a}\tan\left(\frac{\pi a}{2t}\right)}\frac{0.923 + 0.199\left(1 - \sin\left(\frac{\pi a}{2t}\right)\right)^4}{\cos\left(\frac{\pi a}{2t}\right)} \tag{4}$$

Additionally, the critical (Griffith) flaw size is calculated using Eqs. (2) and (3), where a shape factor $Y = {}^2/_{\sqrt{\pi}}$ is applicable according to Ref. [32].

2.6. Density functional theory interface fracture toughness calculation

Density functional theory (DFT), as implemented in the Vienna Ab initio Simulation Package, was used to calculate mechanical properties of the Al-Cr-N system [33,34]. The exchange and correlation effects were described at generalised gradient approximation (GGA) level as parametrised by Perdew-Burke-Ernzerhof [35] while the ion-electron interactions were described employing Projected Augmented Wave pseudo-potentials [36]. The plane wave cut-off energy was to 700 eV and a Monkhorst-Pack mesh [37] of $5 \times 5 \times 1$ k-points was used. Supercells were created by stacking unit cells of wurzite or cubic AlN and CrN along the z-axis. The hexagonal w-[0001] and c-[111] axes were orientated along the z-axis of the reference frame, thus creating a w-(0001) or c-(111) interface in the middle of the supercell, dividing two regions with an equal number of atoms. The calculations were done with cells of 96 atoms. CrN was considered in its anti-ferromagnetic state [38]. Before cleaving the cells to determine the interface strength, they were relaxed until the energy and the forces changes were smaller than 10^{-5} eV (per supercell) and 10^{-2} eV/Å.

The strength of the interface of the relaxed cells was determined either by cleaving at the interface or at an arbitrary plane in the case of the binaries. The cells were separated stepwise, not allowing any relaxation for either the lattice parameters nor the atom positions during cleaving. The creation of two surfaces, due to the separation, leads to an energy increase compared to the relaxed state. The energy difference between the fully separated and the initial intact (bulk) state is considered as the cleavage energy Q_c. Fitting Eq. (5) to the energy (per surface area) vs separation data, one can calculate the critical length (l_c) [39].

$$Q(x) = Q_c\left[1 - \left(1 + \frac{x}{l_c}e^{-\frac{x}{l_c}}\right)\right]. \tag{5}$$

Using the cleavage energy and the Young's moduli E_{hkl} the fracture toughness (K_{IC}) was calculated according to [32]

$$K_{IC} = \sqrt{2\gamma E_{hkl}}, \tag{6}$$

where γ is the surface energy which was approximated by $\gamma = Q_c/2$. E_{hkl} is the directional Young's modulus calculated using literature data.

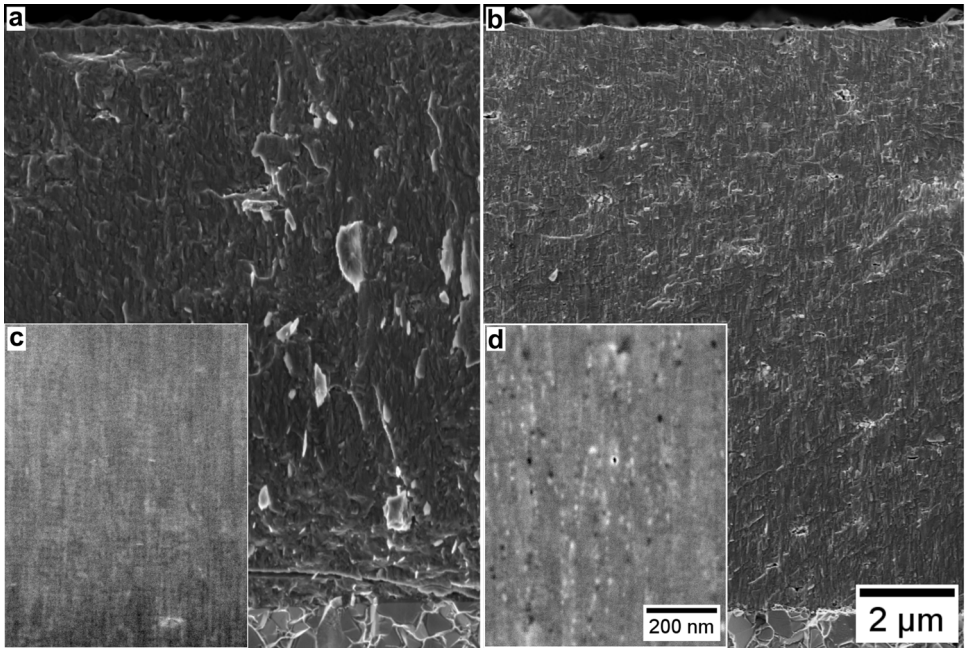

Fig. 1. SEM-micrographs of fracture cross-sections of as-deposited (a) and annealed (b) arc-evaporated films, respectively. The insets with FIB-polished cross-sections (c,d) document a periodic change in the composition in the out-of-plane films' direction. Additionally, formation of globular precipitates at the grain boundaries and at the (formerly Cr-enriched) sublayers' interfaces can be observed in (d).

3. Results

3.1. SEM characterization of as-deposited and annealed microstructure

Representative cross-sections of as-deposited and annealed films are presented in Fig. 1a and b, respectively. In both cases, dense columnar grain microstructures were found at low SEM resolution, whereas the annealed film cross-section shows more submicron cross-sectional features (*cf.* Fig. 1b). The FIB-polished cross section of the film in as-deposited state at low magnifications presented in Suppl. Fig. 1a confirmed the dense microstructure and revealed droplets of different sizes originating from the arc evaporation process disturbing the uniform coating growth (*e.g.* [40,41]). These droplets are either crystalline or amorphous [41] and may also form voids (*cf.* Suppl. Fig. 1a) in agreement with Refs. [40–42]. The further investigation of the FIB-polished cross sections at high magnifications revealed a layered sub-structure with a layer periodicity of ∼30 nm in the as-deposited film (Fig. 1c), typical for the film growth on substrates rotating periodically in and out the line-of-sight of the deposition [43–48]. Eriksson *et al.* identified this effect as preferential resputtering of light elements by heavier ions at high plasma incidence angles, found in segments of the rotation leading to and away from the line-of-sight [43]. In the annealed film at low resolution, some pores could be identified, similar in sizes to the droplets found in as-deposited state (*cf.* Suppl. Fig. 1). The pores are attributed to (i) the higher coefficient of thermal expansion of the metalloid particles and (ii) crystallization of the droplets at high temperatures [49], leading to a densification of the droplets and subsequent formation of an insignificant number of pores (*cf.* Suppl. Fig. 1b). At high magnifications, the cross-sectional layered morphology is still preserved to some extent and, additionally, fine dispersed precipitations were detected (*cf.* Fig. 1d). Groups of the precipitates are distributed along the film in-plane and out-of-plane directions at the intracrystalline sub-layers' interfaces and columnar grain boundaries, respectively (Fig. 1d). From the FIB-cross section presented in Fig. 1d it appears, that the precipitates at the grain boundaries are larger compared to those at the interfaces between the intracrystalline sub-layers. Since the resolution of the SEM images is too low to determine the size of the precipitates accurately, which will be the focus of the TEM and APT analyses presented in Sections 3.3 and 3.4, respectively. Results of EDS performed on the surfaces of the as-deposited and annealed films are presented in Table 1 and indicate that, (i) within the accuracy of the method, the overall film composition did not change after the annealing and (ii) there was only small amount of residual O from the dilatometer chamber (Section 2.2) incorporated into the film during annealing. Regarding the quantification of the O content in the film interior, the results obtained by APT (Section 3.4.) should be considered, where a total O content below 0.2 and 0.5 at.% was detected for the as-deposited and annealed films, respectively. Furthermore, the EDS results revealed, that the Cr/(Al+Cr) ratio is slightly higher compared to the cathode composition of $Al_{0.9}Cr_{0.1}$ (Section 2.1), which can be related to the preferential scattering and sputtering of the lighter Al compared to the heavier Cr [50].

3.2. Indentation, in situ *micromechanical testing and* ex situ *fractography*

As a next step, the influence of the precipitation observed in SEM, data (*cf.* Fig. 1) on the mechanical properties of the as-deposited and annealed w-AlCrN films was further analyzed. Hardness H and indentation modulus E_i were determined by the nanoindentation and the data are summarised in Table 2. Though moderate values were detected in the as-deposited film compared to the literature [51,52], an increase of 6 and ∼90 GPa (both ∼35%) detected after the heat-treatment for H and E_i, respectively, is quite remarkable.

In order to assess the mechanical properties without an influence of residual stresses and the substrate, micromechanical bending tests on notched and unnotched cantilevers were performed. The recorded load-deflection curves (*cf.* Fig. 2a and b, respectively) reveal a linear-elastic deformation, *i.e.,* no signs of plastic deformation were observed. The curves were utilised to evaluate E, σ_F and

Table 1
Elemental composition of the film in as-deposited and annealed state, respectively.

	Al [at.%]	Cr [at.%]	N [at.%]	O [at.%]	Cr/(Al+Cr) [-]
as-deposited	43.9 ± 2.2	6.6 ± 0.6	48.6 ± 2.8	0.9 ± 0.7	0.131 ± 0.018
annealed	43.6 ± 1.5	6.5 ± 0.4	48.1 ± 1.5	1.8 ± 0.6	0.130 ± 0.012

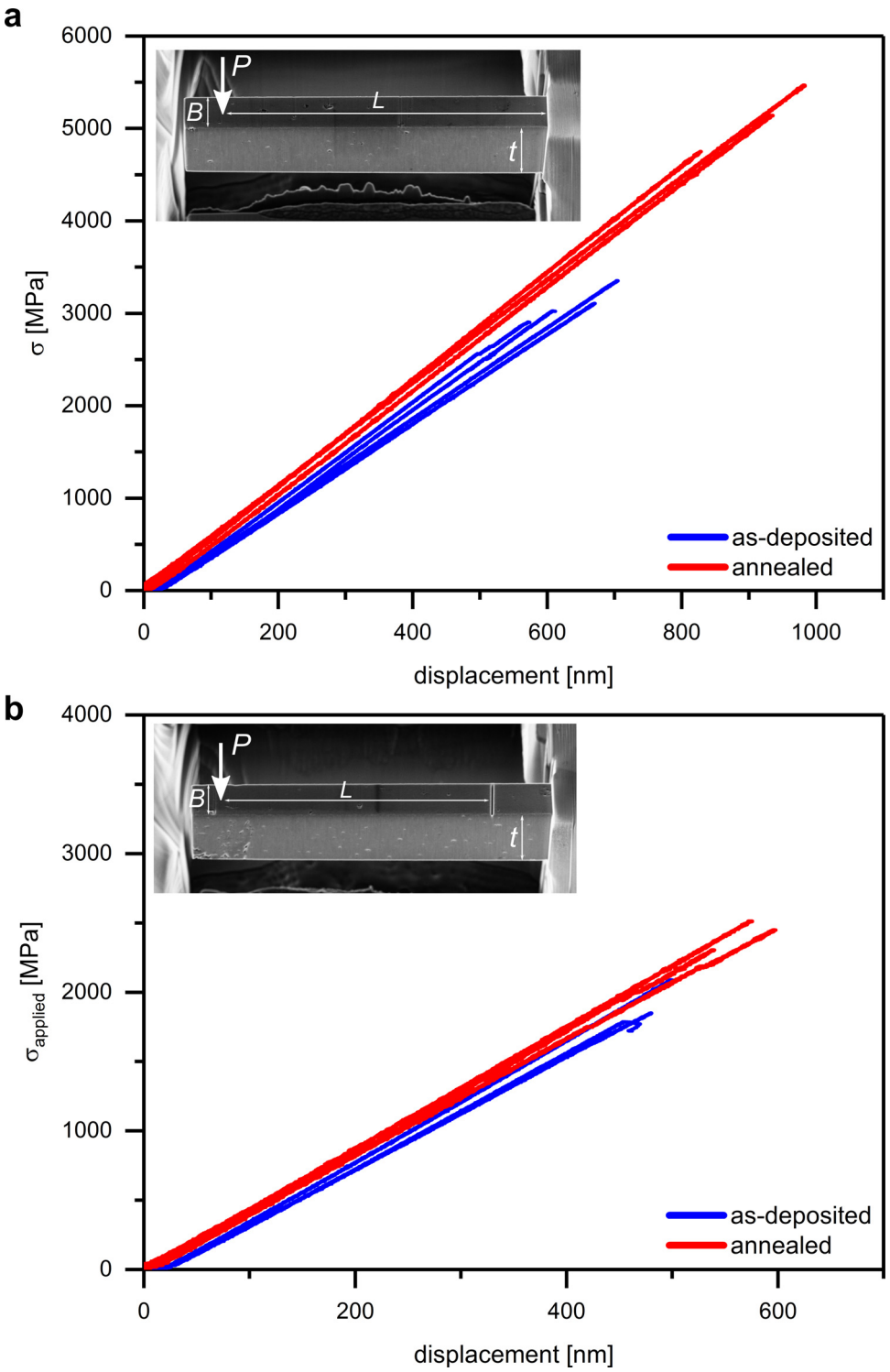

Fig. 2. Load-deflection curves recorded during micromechanical tests on unnotched (a) and notched (b) cantilevers FIB machined from as-deposited and annealed films. The inserts in (a) and (b) represent the unnotched and notched cantilever geometry, respectively with $L \times B \times t$ dimensions of $\sim 12 \times 2 \times 2.9\,\mu m^3$.

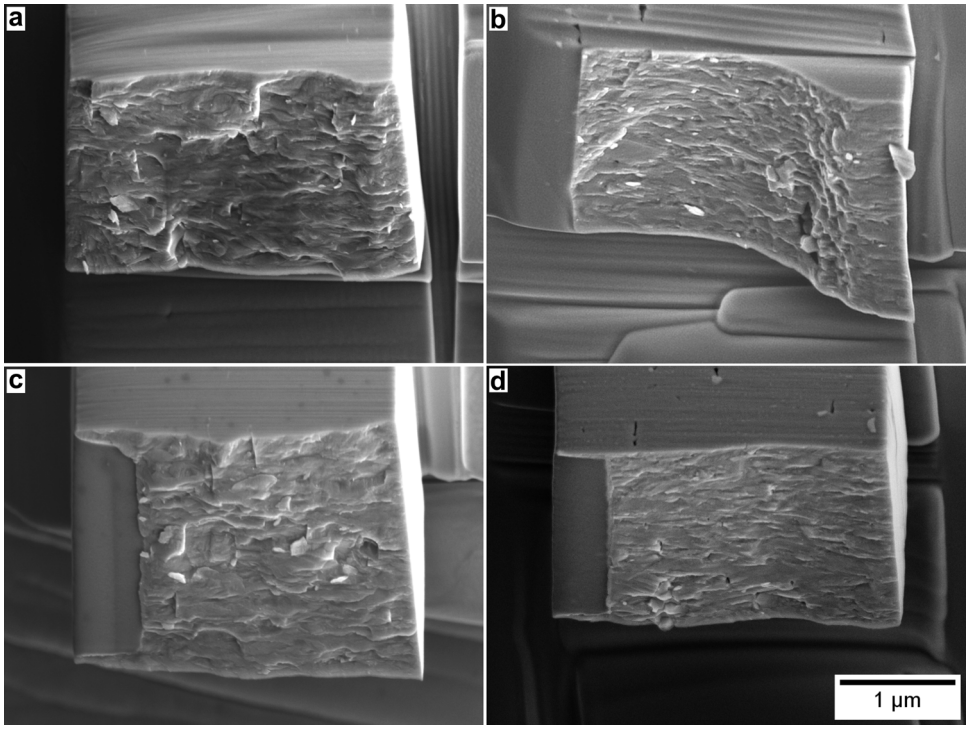

Fig. 3. Fracture surfaces of unnotched cantilevers fabricated from as-deposited (a) and annealed films (b); fracture surfaces of notched cantilevers fabricated from as-deposited (c) and annealed films (d). The as-deposited film (a,c), fractures along columnar grain boundaries. The annealed film (b,d) shows the relatively smooth wavy fracture surfaces indicating a transgranular fracture. Additionally, the S-shaped fracture path in (b) is a further indication for transgranular film cracking.

Table 2
Hardness (H) and indentation modulus (E_i) in as-deposited and annealed state measured by means of nanoindentation.

	H[GPa]	E_i[GPa]
as-deposited	18.3 ± 1.0	251 ± 16
annealed	24.3 ± 1.0	343 ± 21

K_{IC} according to Eqn 1, 2, 3 and 4 (*cf.* Section 2.5), which are summarised in Table 3.

The Young's modulus E derived from the bending experiment is in good agreement with the data evaluated by indentation tests (*cf.* Tables 2 and 3), again an increase from ~210 to 310 GPa was found for the as-deposited and annealed states, respectively. The differences between the particular moduli (received from nanoindentation and cantilever-bending experiments) on the two films can be attributed to substrate effects and gradient nature of the columnar films.

A significant increase after the annealing was also found for the fracture stress σ_F, which reached a value of 5.1 GPa, only inferior to CrN in as-deposited state, yet superior to the same film after annealing to 500°C [9] and far beyond previously reported fracture stress values of other monolithic or even advanced PVD nitride thin films reported in Refs. [2,8].

Finally, a slight increase of facture toughness K_{IC} by ~10% was evaluated from the cantilever experiments after the annealing. However, an increase in the film's fracture resistance can be represented also by the critical flaw size. According to Eq. (3) (*cf.* Section 2.5), a change of the natural critical flaw size from 178 ± 59 to 87 ± 18 nm after annealing was evaluated from the fracture stress and fracture toughness.

However, there is a remarkable difference in the morphology of the fracture surfaces of the as-deposited and annealed $Al_{0.9}Cr_{0.1}N$ films shown in Fig. 3. In the as-deposited microcantilevers (Fig. 3a,c), an intercolumnar fracture was observed, indicated by the rather rough fracture surface originating from the microscopic changes of the crack path along the boundaries of the columnar grains, similar to the fracture cross-section presented in Fig. 1a. This behavior is typical for PVD transition metal nitride thin films and is in a good agreement with the literature [2,3,6]. Contrary, in the annealed unnotched and notched microcantilevers presented in Fig. 3b and 3d, respectively, rather smooth and wavy fracture surfaces were found. Moreover, in the case of the unnotched cantilever (Fig. 3d), an S-shaped contour along the fracture path, which is in general associated with trans-columnar fracture during bending (*i.e.* a change in the fracture path to regions with less compressive stress in the lower half of the remaining cantilever), as seen for example for single-crystalline Si [53] or defect-free WC [54], was detected.

It is expected that the change in fracture surface morphology from inter-columnar to trans-columnar fracture is related to the formation of c-Cr(Al)N nano-precipitates along the (formerly Cr-enriched) sublayers' interfaces and at the columnar grain boundaries, which nature and origin will be further discussed in detail in Sections 3.3–3.5, which are devoted to TEM, APT and *in situ* HE-HT-GIT-XRD. The precipitates presumably block the normally weak fracture links along the grain boundaries, which is supported by qualitative results obtained via ab initio DFT calculations (*cf.* Section 3.6).

3.3. TEM characterization

EDS was performed in TEM on the as-deposited and annealed films cross-sections to obtain further insights onto the nanoscopic elemental distributions of Cr, Al and N in the precipitates and in the matrix (Fig. 4) contributing to the unprecedented fracture behavior for w-AlCrN films presented above. The HAADF micrograph and the corresponding elemental color maps retrieved from the as-deposited film (Fig. 4a) show a cross-sectional periodic variation of

Table 3
Mechanical properties investigated by *in situ* cantilever bending tests in as-deposited and annealed state.

	E[GPa]	σ_F[GPa]	K_{IC}[MPa $m^{1/2}$]	critical flaw size [nm]
as-deposited	212 ± 18	3.2 ± 0.4	2.7 ± 0.3	178 ± 59 (141–226)
annealed	311 ± 18	5.1 ± 0.4	3.0 ± 0.2	87 ± 18 (75–100)

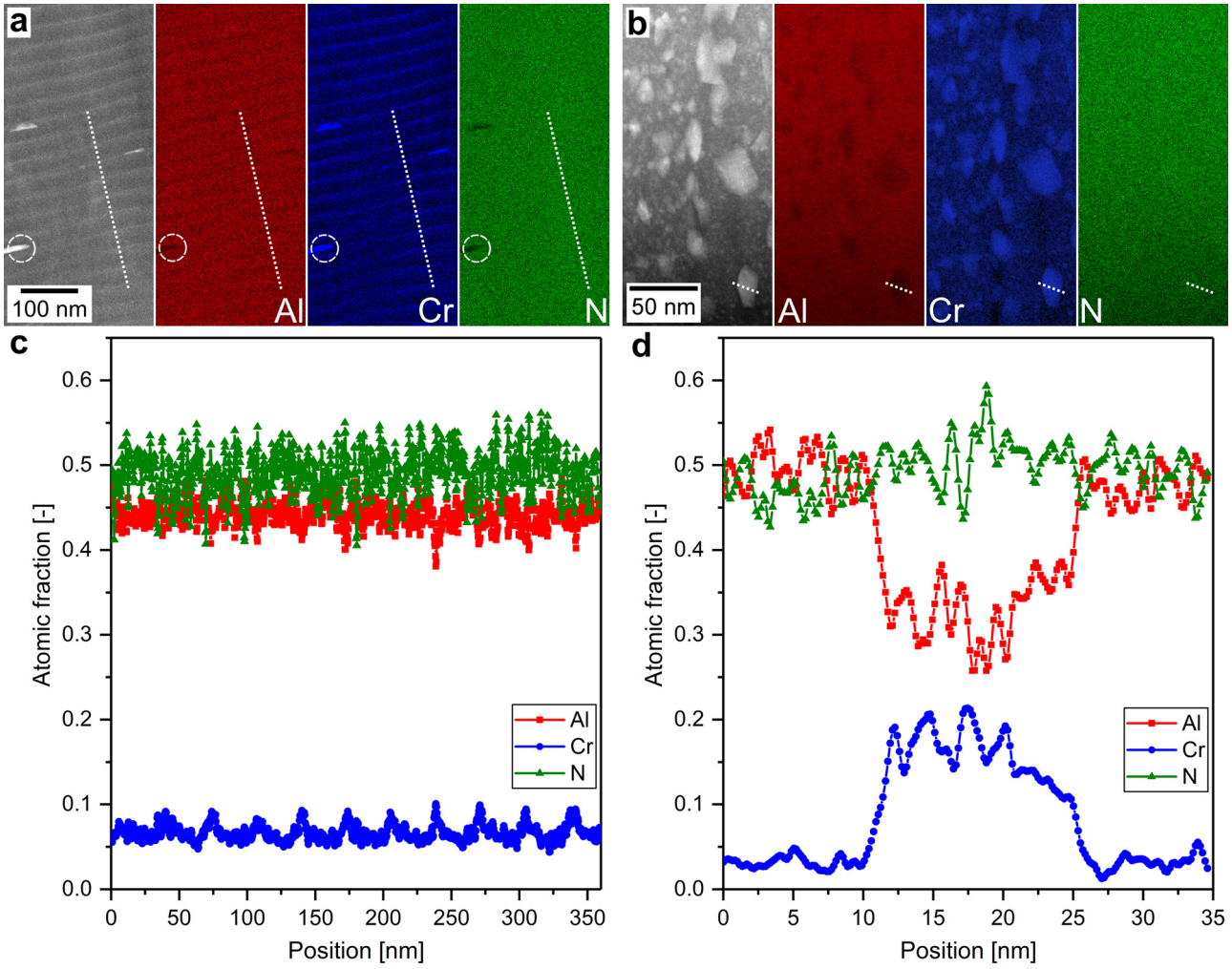

Fig. 4. Results from HAADF and EDS analyses on the as-deposited (a,) and annealed (b,d) AlCrN thin films. The elemental composition along the dashed lines in (a,b) is presented in (c,d). The results indicated a periodic variation of Cr and Al in the as-deposited arc-evaporated film and complementary Cr-enrichment/Al-depletion across a representative precipitate in the film after the annealing. The N composition in both films appear monotonous and unchanged by the thermal treatment. The dashed circles in (a) indicate a microdroplet differing in chemical composition, especially a depletion in N.

Al and Cr concentrations, while the N content in the film remains constant.

Furthermore, a quantitative line intersection presented in Fig. 4c reveals that the sublayers' interfaces are already enriched in Cr with an excess magnitude of ~9 at.% compared to sublayers' interiors, where ~5.5 at.% Cr-content was detected, accompanied by a complementary deficiency of the Al-content. Additionally, micro- and nanodroplets were incorporated in the film in the as-deposited state, which could be clearly detected due to their depletion in N (*cf.* the encircled area in the Al, Cr, and N maps in Fig. 4a) [40,55,56]. Due to the intrinsic roughness of the arc-evaporated film induced by these micro- and nanodroplets, the actual periodic elemental variation may be covered. Therefore, the 3D APT results from Fig. 7 should be considered for better resolution.

Chemical analysis performed on the annealed film cross-section is presented in Fig. 4b and d. The HAADF micrograph and the elemental maps clearly reveal that the angular precipitates are depleted in Al and enriched in Cr, whereas N was evenly distributed within the scanned area (Fig. 4b). A variation of chemical composition along a representative precipitate is furthermore highlighted in Fig. 4d, where the Cr-content is enriched to ~0.2, whereas Al-content is reduced to ~0.3 far off the overall concentration presented in Table 1. Remarkably, the concentrations of both metals and N oscillate reciprocally along the precipitate (Fig. 4d). However, an influence of the (possibly) underlying w-AlCrN matrix on the results cannot be fully excluded, therefore the individual composition of selected precipitates was further analyzed by APT in Section 3.4.

In order to investigate the cross-sectional microstructure of the films further, HR-TEM was performed. An elongated ~15 nm thick grain within the as-deposited film was selected in bright field mode (appearing dark in Fig. 5a) and imaged by HAADF (Fig. 5b) and HR-TEM (Fig. 5c). Several brighter Cr-enriched zones cross the

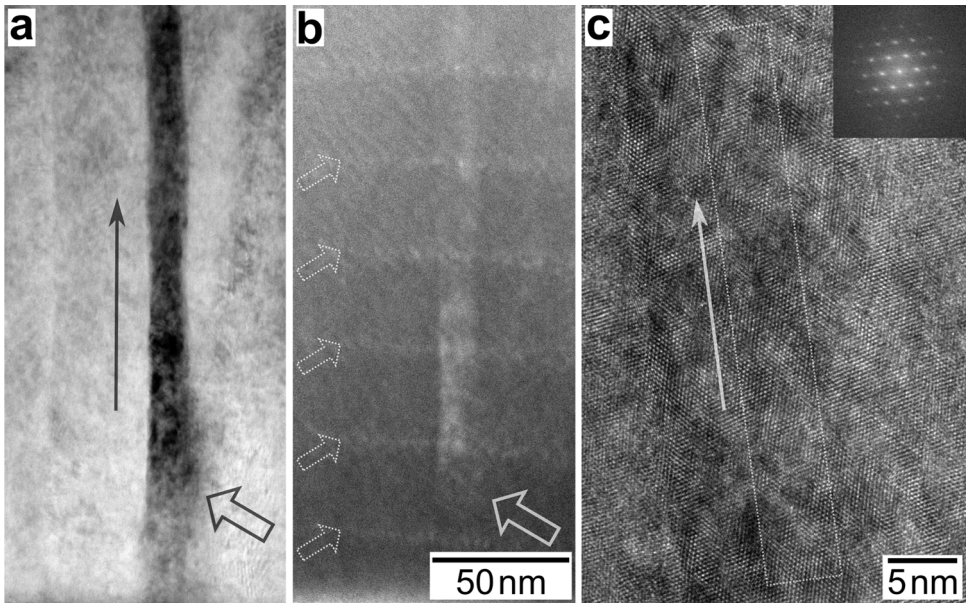

Fig. 5. TEM-analysis of the as-deposited AlCrN thin film. A bright-field STEM micrograph showing the elongated columnar grains is presented in (a). The marked dark grain fulfils the diffraction condition and is bright in (b) and imaged using HR-TEM in (c). A HAADF STEM micrograph is presented in (b), the dashed arrows showing the periodic modulation of Cr content, while the bright grain is imaged using HR-TEM in (c). HR TEM analysis of the film in as-deposited state (c). The inset shows the FFT produced from the dashed rectangle. The arrows in (a) and (c) indicate the film growth direction. Please note that the scalebar in (b) applies for both (a) and (b).

grain (*cf.* Fig. 3b), with a period of ~34 ± 0.5 nm, in agreement with the EDS data from Fig. 4a and c. The same grain was imaged by HR-TEM, where the fast Fourier transformation (FFT) indicates exclusively wurtzite crystal structure and the [110] orientation to be parallel to the growth direction (Fig. 5c), in agreement with the X-ray diffraction data obtained from the sample (*cf.* Section 3.5).

The cross-sectional microstructure of the annealed sample (*cf.* Fig. 6a) is dominated by rather globular precipitates formed at the intracrystalline interfaces between the sublayers (formerly Cr-enriched regions, *cf.* Fig. 5b) and elongated precipitates formed at the columnar grain boundaries. Additionally, metallic globular micro-droplets (encircled in Fig. 6) originating from the arc evaporation process are still present within the film. The corresponding EDS map and line-intersection along the micro-droplet are shown in Suppl. Fig. 2. In agreement with Fig. 1d, it can be qualitatively concluded from Fig. 6a, that the elongated precipitates formed at the columnar grain boundaries (indicated by dashed arrows) are larger compared to those formed at the Cr-enriched zones (solid arrows) within the grains. Additionally, the HR-TEM, FFT and selected electron diffraction analyses of a representative precipitate at a grain boundary in Fig. 6b indicate the presence of cubic phase precipitate and wurtzite matrix (*cf.* Fig. 6b,c). The individual chemical composition of the selected precipitates was quantified by APT and is presented in the following section.

3.4. APT characterization

In order to get further insight into the local chemical composition of the matrix and the precipitates in both the as-deposited and annealed films, APT was performed (*cf.* Figs. 7 and 8). The as-deposited film exhibits a periodic increase in Cr concentration, represented by the isoconcentration surfaces in Fig. 7a, whereby peak Cr concentrations of ~8 at.% were found with a periodicity of 34 nm (Fig. 7b) along the growth direction, accompanied by a complementary Al depletion. No clustering or depletion was found for N and no clusters of enhanced Al content were detected in the as-deposited film (Fig. 7). The oxygen content was <0.2 at.% and the variation in Cr content between 5 and 8 at.% is in good agreement with the EDS data received from SEM (Table 1) and TEM (Fig. 4). Corresponding mass spectrum data is provided in Suppl. Fig. 3 together with a detailed list in Suppl. Table 1 of the employed ranging which corresponds to the assignment of chemical species to the detected peaks. From the mass spectrum data, it is obvious that the $^{54}Cr^{2+}$ isotope overlaps with $^{27}Al^{+}$. The entire peak at 27 Da was assigned to Al and based on the Cr abundance it can be determined that the underestimation of the Cr content is maximum 0.2 at.% and thus negligible.

However, the N content varies between 39 and 43 at.% along the composition profile and is significantly lower than the 49 at.% obtained by EDS. Consequently, the absolute N composition, quantified by laser-assisted APT is underestimated, while Al is overestimated. Laser-assisted APT quantification of a $(Ti_{0.255}Al_{0.235})(N_{0.505}O_{0.005})$ thin film at 10 pJ laser pulse energy revealed underestimation of N by 4.1 to 5.6 at.%, while Al was overestimated by 3.0 to 4.5 at.% [23,24]. These compositional discrepancies can be understood by dissociation of N_2-carrying molecular ions resulting in neutral fragments which cannot be detected [57]. As the (Cr,Al)N and (Ti,Al)N systems are similar in terms of bond strength [58], it can be expected that the nitrogen content of the here investigated $Al_{0.9}Cr_{0.1}N$ films is underestimated by up to 5 at.%, when quantification is based on laser-assisted APT.

The APT results from the annealed sample are presented in Fig. 8 and the oxygen content was <0.5 at.%. Primarily, *two types of elemental clusters* could be identified, which are (i) Cr-enriched clusters with the size of <~10 nm regularly distributed in the probed volume and (ii) elongated, considerably larger clusters composed of Cr and N and completely depleted of Al. The smaller clusters (Fig. 8a,b) represent the precipitates formed within the columnar grains at the interfaces between the (formerly Cr-enriched) sublayers' interfaces (*cf.* full arrows in Fig. 6a), which are composed of $Al_xCr_{1-x}N$ with an Al-content far below the experimental limit of $x \approx 0.7$ [51,59] for the stabilization of the cubic phase. The larger elongated clusters, which are exclusively formed of Cr and N (*cf.* Fig. 8c), represent c-CrN precipitates formed along the boundaries of the columnar grains (*cf.* Fig. 6c).

Furthermore, a Cr cluster (Fig. 8d) depleted in Al and N, was identified in vicinity of AlN, depleted in Cr. Following, this clus-

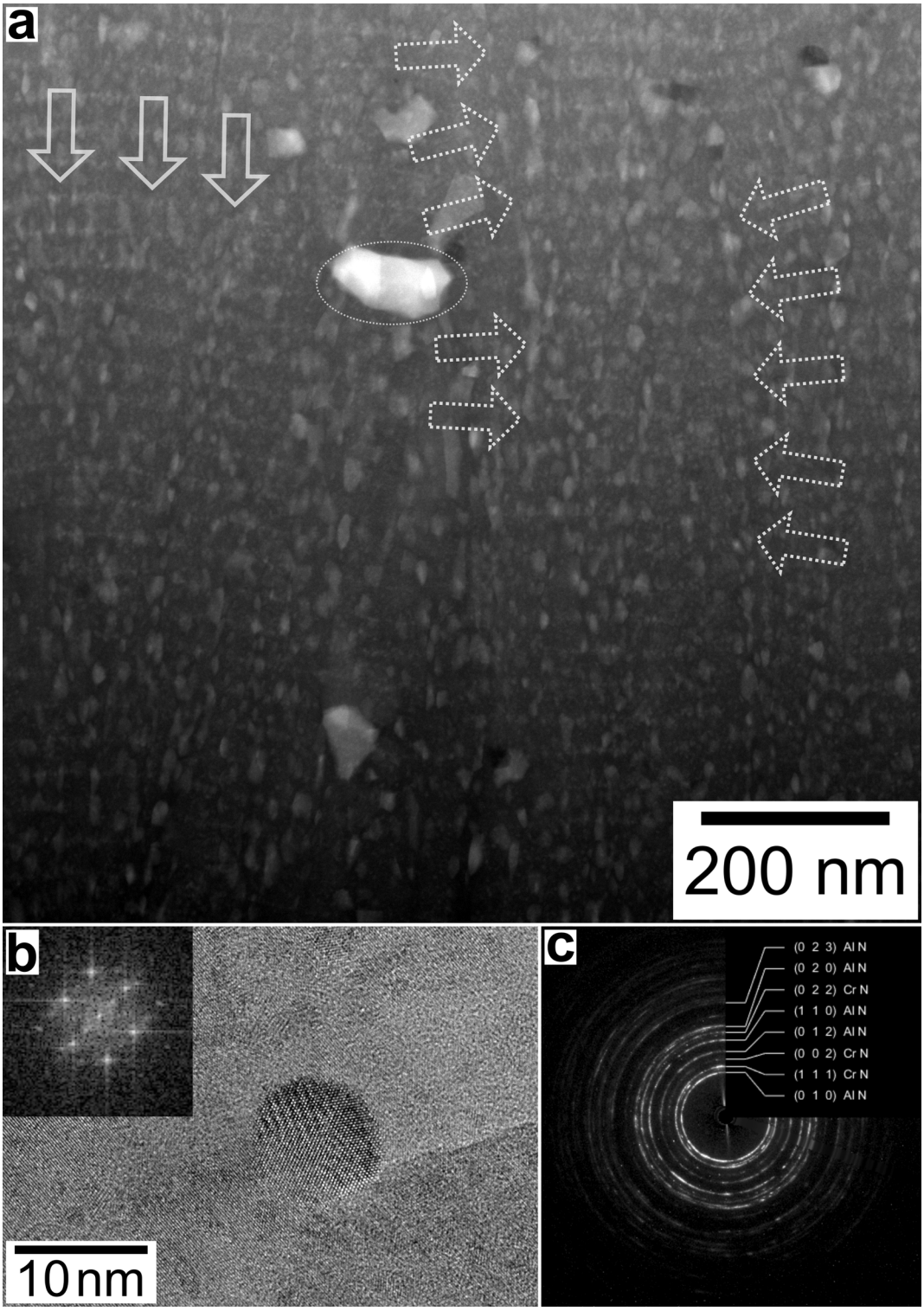

Fig. 6. TEM-analysis of the annealed AlCrN film. HAADF micrograph in (a) shows the precipitates formed at the (formerly Cr-enriched) sublayers' interfaces (exemplary marked with full arrows) and at the columnar grain boundaries (dashed arrows). The encircled particle is a microdroplet originating from the deposition process. In (b), HR-TEM of a representative c-Cr(Al)N precipitate at a grain boundary fulfilling the diffraction condition, the inset shows the FFT of the precipitate. SAED of the annealed film identifies w-AlN and c-CrN phases present after the annealing (c).

ter is identified as a micro-droplet originating from the deposition process in agreement to TEM results (Fig. 4) and literature [40,55,56]. The uncertainties induced by atom probe data reconstruction were minimized through tuning the reconstruction parameters based on TEM data towards a bilayer thickness of 34 nm in case of the as-deposited thin film. As shown in Suppl. Fig. 4, the as-deposited and annealed specimens employed for atom probe measurements look very similarly after FIB preparation. Hence, the reconstruction parameters from the as-deposited film were similarly adopted for the annealed one. Thus, the reconstructed sizes of the precipitates can be expected to be on the right order of magnitude.

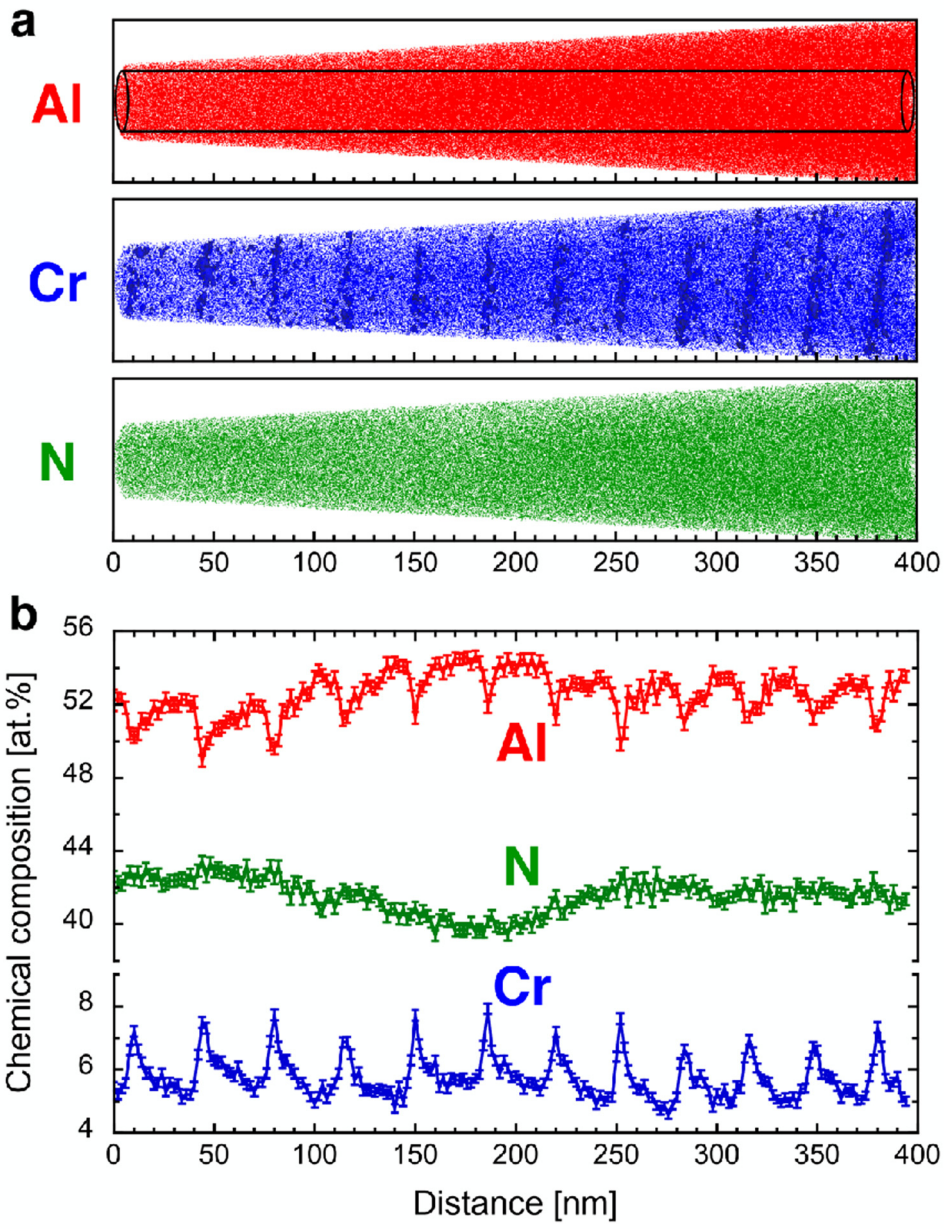

Fig. 7. APT characterization of the $Al_{0.9}Cr_{0.1}N$ thin film in as deposited state. Al, Cr and N atomic positions are presented in (a) with isoconcentration surfaces highlighting regions with Cr ≥10 at.%. Concentration profiles for Al, Cr and N along the cylinder in (a) are presented in (b), showing periodic depletion and enrichment of Al and Cr, respectively, in good agreement with TEM-EDS data presented in Fig. 4.

3.5. In situ *high-temperature high-energy X-ray diffraction analysis*

In order to understand the temperature-dependent decomposition pathways within the w-AlCrN thin film, *in situ* high-temperature X-ray diffraction was used to assess volume-averaged properties. The results from the *in situ* synchrotron experiment were used to assess primarily the phase evolution, in-plane residual stresses and microstructure within the $Al_{0.9}Cr_{0.1}N$ film during annealing in the range of 25–1100°C (Fig. 9a), applying the methodology from Ref. [21]. The aim was to identify structural changes, which might influence the mechanical behavior of the annealed film. A portion of the experimental data as well as the evaluation methodology are presented in the supplementary information.

At room temperature, film wurtzite Al(Cr)N 100, 002, 101, 102 and 110, substrate hexagonal WC 100 and 101 as well as substrate cubic Co 111 and 200 reflections were recorded by the 2D detector [60]. During the heating up and cooling down, the peaks shifted collectively to lower and higher diffraction angles, respectively, due to thermal expansion and contraction of the crystal lattice (Fig. 9b). After passing the deposition temperature threshold, peak widths of the Al(Cr)N reflections gradually decreased and intensities increased, as a consequence of the structure recovery [11]. No signal from the c-Cr(Al)N and c-CrN precipitates could be however detected, due to the small size of the precipitates resulting to relatively small scattering cross-sections and the fact, that in the particular 2θ-region, the c-Cr(Al)N 111 and 200 reflections were mainly overlapped with the w-AlN 101 and c-Co 111 reflections, respectively.

In situ qualitative texture analysis was performed by evaluating azimuthal intensity distributions along Debye-Scherrer rings, as discussed in the supplementary data. The results revealed a mix-

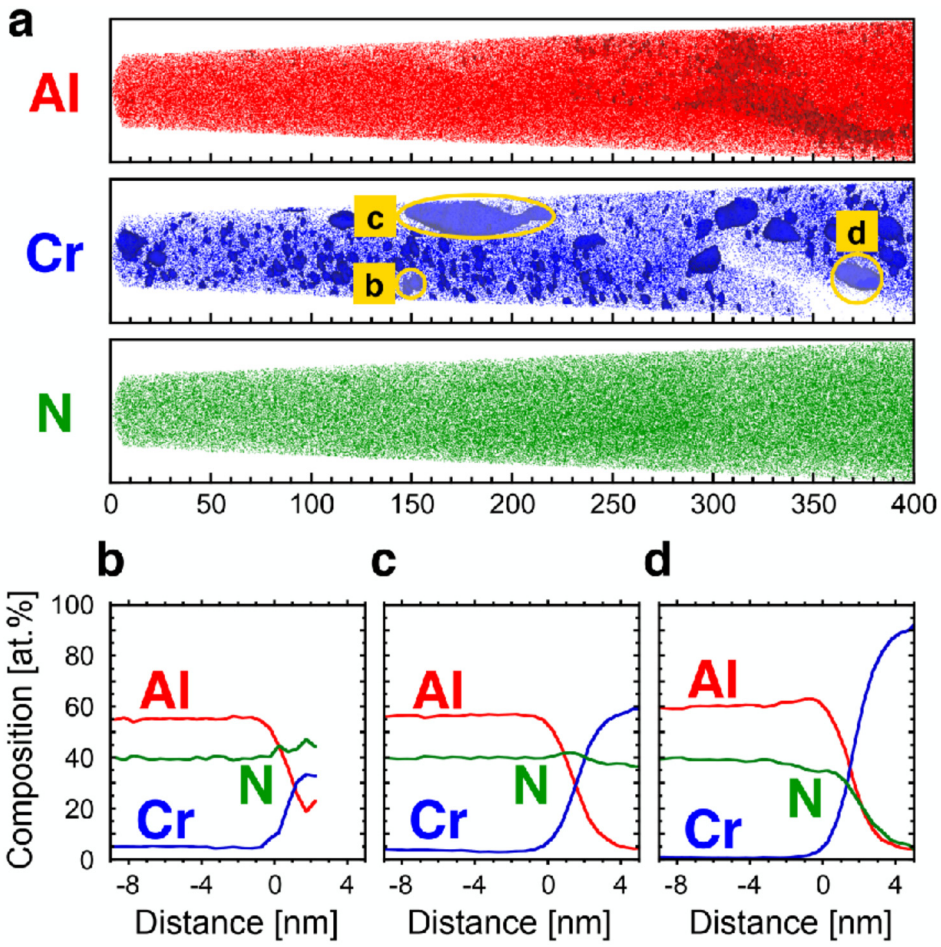

Fig. 8. APT characterization of the $Al_{0.9}Cr_{0.1}N$ thin film after annealing at 1100°C. Al, Cr and N atomic positions are presented in (a), with isoconcentration surfaces highlighting regions with Al ≥65 at.% Cr ≥10 at.%. Proximity histograms of Cr-rich regions with Cr ≥10 at.% are presented for selected precipitates in (b), (c) and (d) and the corresponding precipitates are highlighted by circles in (a). It can be seen, that three different types of precipitates evolve during the heat treatment, which are rather globular AlCrN precipitates with a size <10 nm within the columnar grains (b), elongated CrN precipitates at the grain boundaries (c) and Cr precipitates corresponding to micro-droplets originating from the deposition process (d).

ture of ⟨100⟩ and ⟨110⟩ fibre textures, both with densely-packed {001} planes oriented parallel to the growth direction as well as to the boundaries of the columnar grains (*cf.* Suppl. Fig. 5). The texture did not change significantly during the annealing.

2D diffraction data were used to evaluate temperature dependencies of the unstressed lattice parameters $c_o(T)$ and $a_o(T)$ using the methodology presented in the supplementary information. In the temperature range of 25–475°C, both c_o and a_o gradually increase with the temperature as a consequence of crystal lattice thermal expansion (Fig. 9c). Above the deposition temperature of ~475°C, however, a_o start to decrease and, at the end of the thermal cycle, a_o shrinks significantly, whereas c_o remains practically unchanged. The a_o shrinkage can be attributed to the diffusion of Cr out of the w-AlCrN lattice, as discussed in Ref. [61]. Interestingly, during the holding segment, the slope $\partial a_o(T)/\partial T$ gradually decreases, which represents a reduction of the Cr segregation out of the lattice due to missing driving force for the further decomposition (Fig. 9c). Contrary, it can be seen, that the *c*-axis of the hexagonal lattice follows the applied temperature profile and no significant changes during the heat treatment could be detected. Following, it can be assumed that Cr was mainly dissolved within the basal planes of the wurtzite crystallites [61].

Additionally, the diffraction data were used to evaluate the temperature dependence of in-plane residual stresses in the film by analysing an ellipticity of w-AlCrN 110 reflection. In the as-deposited state, the residual stress was -5.1 ± 0.1 GPa. Upon heating up in the temperature range of 25–475°C, the compressive residual stress stayed nearly constant due to the slight difference in coefficients of thermal expansion (CTEs) of w-AlCrN and the substrate (Fig. 9d) [21,62]. Above the deposition temperature, however, residual stress gradually relaxed reaching a magnitude of -0.9 ± 0.1 GPa at 1100°C, due to microstructure recovery and defect annihilation [11], represented also by the complementary full width at half maximum (FWHM) changes in Fig. 10. During the cooling down, the compressive residual stress again slightly increases to -1.1 ± 0.1 GPa, once more due to the CTEs mismatch. It should be noted that the compressive residual stress with typical intrinsic and extrinsic stress contributions is not expected to significantly influence fracture properties of the free-standing micro-cantilevers analyzed further in Section 3.2 (*cf.* also Figs. 2,3).

Additionally, the FWHM evolution of w-AlCrN 100 reflections was evaluated for in-plane and out-of-plane diffraction vector orientations. Generally, FWHM of XRD peaks correlates with the size of coherently diffracting domains as well as with the density of structural defects such as dislocations and lattice distortions, represented by strains of 2nd and 3rd order [63]. Since the w-AlCrN crystallites exhibited columnar grain morphology (*cf.* Figs. 1,5,6), which did not change significantly during the thermal treatment, it can be assumed that the FWHM changes can be primarily at-

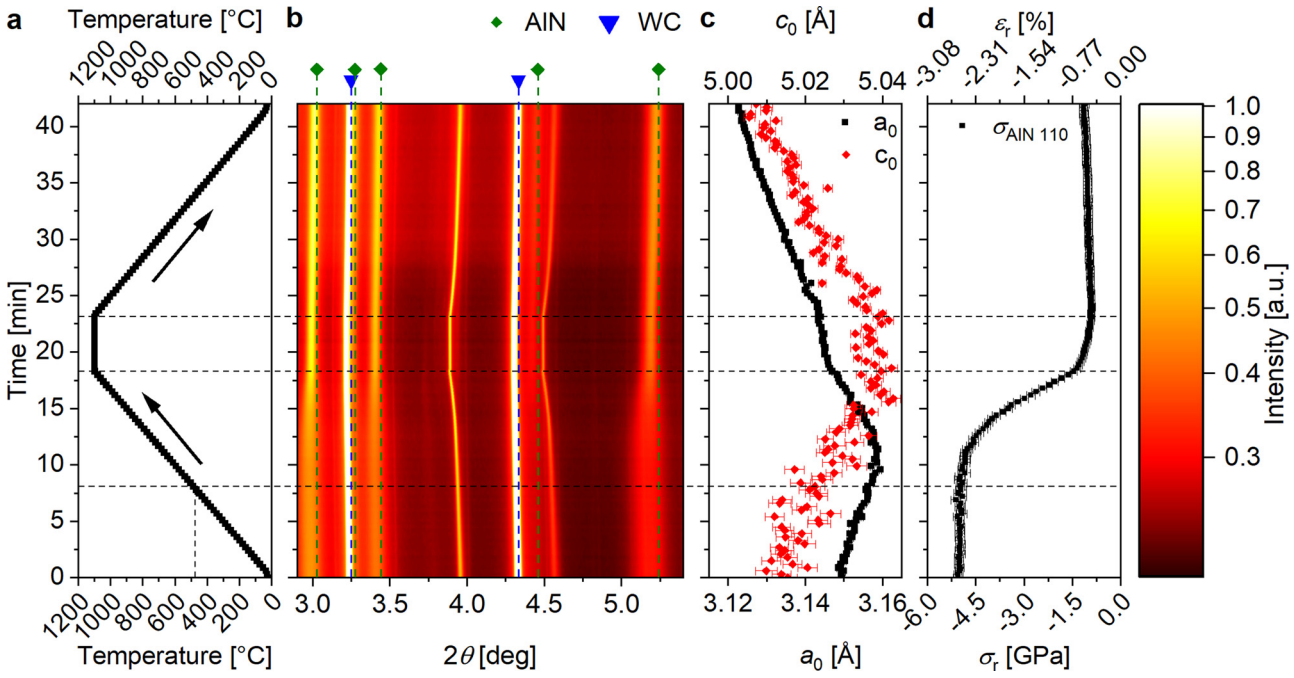

Fig. 9. Results from *in situ* high-temperature high-energy grazing incidence diffraction analysis on the $Al_{0.9}Cr_{0.1}N$ thin film. The applied temperature cycle (a), the wide-angle X-ray diffraction phase plot showing wurtzite AlN thin film phase and WC-substrate (b), the in-plane residual stress and strain evolution (c) and the evolution of a_0 and c_0 lattice parameter (d) are presented. The dashed and dotted lines indicate the deposition temperature of 475°C and the beginning and end of the holding segment, respectively.

tributed to the variation of structural defect density and precipitate formation. The FWHM results in Fig. 10 indicate a columnar grained microstructure, which is reflected by relatively small and large FWHMs (*i.e.* large and small sizes of coherently diffracting domains) in out-of-plane and in-plane diffraction vector orientations, respectively, in the as-deposited film. Up to the deposition temperature of 475°C, both FWHMs decrease only slightly due to the insufficient driving force for a diffusion-driven defect annihilation. After passing the deposition temperature, however, the out-of-plane FWHM increases significantly due to the Cr segregation at the (formerly Cr-enriched) sublayers' interfaces within the columnar grains, which results in the generation of strain fields and probably also in the deterioration of the coherency of the out-of-plane diffracting crystallites. The further heating up results in the Cr agglomeration and the formation of c-Cr(Al)N precipitates (Fig. 6b), for which the temperature threshold however cannot be exactly determined. Further temperature increase results in the annihilation of growth defects, originating from the deposition process, and the out-of-plane FWHM starts to decrease at the temperature of ~900°C [11], in agreement with the residual stress data from Fig. 9d. In the case of in-plane FWHM, only the latter effect is relevant for its thermal behavior. The small difference in the out-of-plane and in-plane FHWMs after the temperature cycles can be attributed to the incoherent precipitates within the columnar grains, which limit the size of coherently diffracting domains in the out-of-plane direction.

3.6. DFT analysis of interfacial strength and toughness

Ab initio DFT calculations were applied to analyse trends in fracture behavior of various phases and interfaces being present in the as-deposited and annealed films. It needs to be stressed that the below presented predictions are not to be directly correlated with experimental values but are merely intended to reveal trends in fracture behavior. Despite the simplicity of Eq. (6) and related calculational approximations, this approach has been proven to be useful for quantifying fracture toughness trends in hard nitride thin films [7,64,65]. In the as-deposited state, the microstructure is dominated by w-AlCrN grains and the grain boundaries are predominantly oriented parallel to {0001}. Considering the experimentally determined chemical composition in Sections 3.1, 3.3 and 3.4, the fracture toughness is approximated with that of w-AlN. The calculations for (0001) fracture surface yielded values of 5.5 J/m^2 and 1.9 MPa m^{½} for the surface energy $\gamma_{(1000)}$ and fracture toughness $K_{IC,(0001)}$, respectively, employing directional Young's modulus based on calculated elastic constants ($E_{[0001]} = 320$ GPa [66]) for the latter. This fracture toughness value is in excellent agreement with $K_{IC} = 1.9$ MPa m^{½} obtained using explicitly calculated surface energy ($\gamma_{(0001)} = 5.8$ J/m^2 [67]) as well as in reasonable agreement with the prediction by Koutná *et al.* $K_{IC} = 2.3$ MPa m^{½} [68]. It is noted that different orientations of fracture planes result in even lower values: $K_{IC,(1\text{-}100)} = 1.2$ MPa m^{½} and $K_{IC,(11\text{-}20)} = 1.6$ MPa m^{½} and surfaces energies $\gamma_{(1\text{-}100)} = 2.3$ J/m^2 and $\gamma_{(11\text{-}20)} = 3.75$ J/m^2. In a following step, the c-Cr(Al)N precipitates are considered. EDS (Fig. 4) and APT (Fig. 8) suggest that their composition varies between c-$Cr_{0.5}Al_{0.5}N$ and c-CrN. Recently published data on c-CrN and c-AlN [65] reveal that K_{IC} increases from 1.3 MPa m^{½} (c-AlN) and 1.6 MPa m^{½} (c-CrN) for (100) surfaces to 2.7 MPa m^{½} (c-AlN) and 2.5 MPa m^{½} (c-CrN) for (110) fracture planes. Using surface energy and directional Young's modulus from the literature suggests even higher K_{IC} values for the (111)-oriented c-AlN [67,69]. Therefore, when the hexagonal (0001) and corresponding cubic (111) fracture surfaces are compared, a higher fracture toughness is predicted for the c-Cr(Al)N phase than the original w-AlCrN. Thereby we propose that the appearance of the Cr-rich cubic phase after the annealing is not detrimental to the fracture behavior. For clarification, all data presented in this section are summarized in Suppl. Table 2.

Finally, focus is drawn on the fracture toughness of the newly created w-AlCrN/c-Cr(Al)N interfaces. Bartosik *et al.* [70] have re-

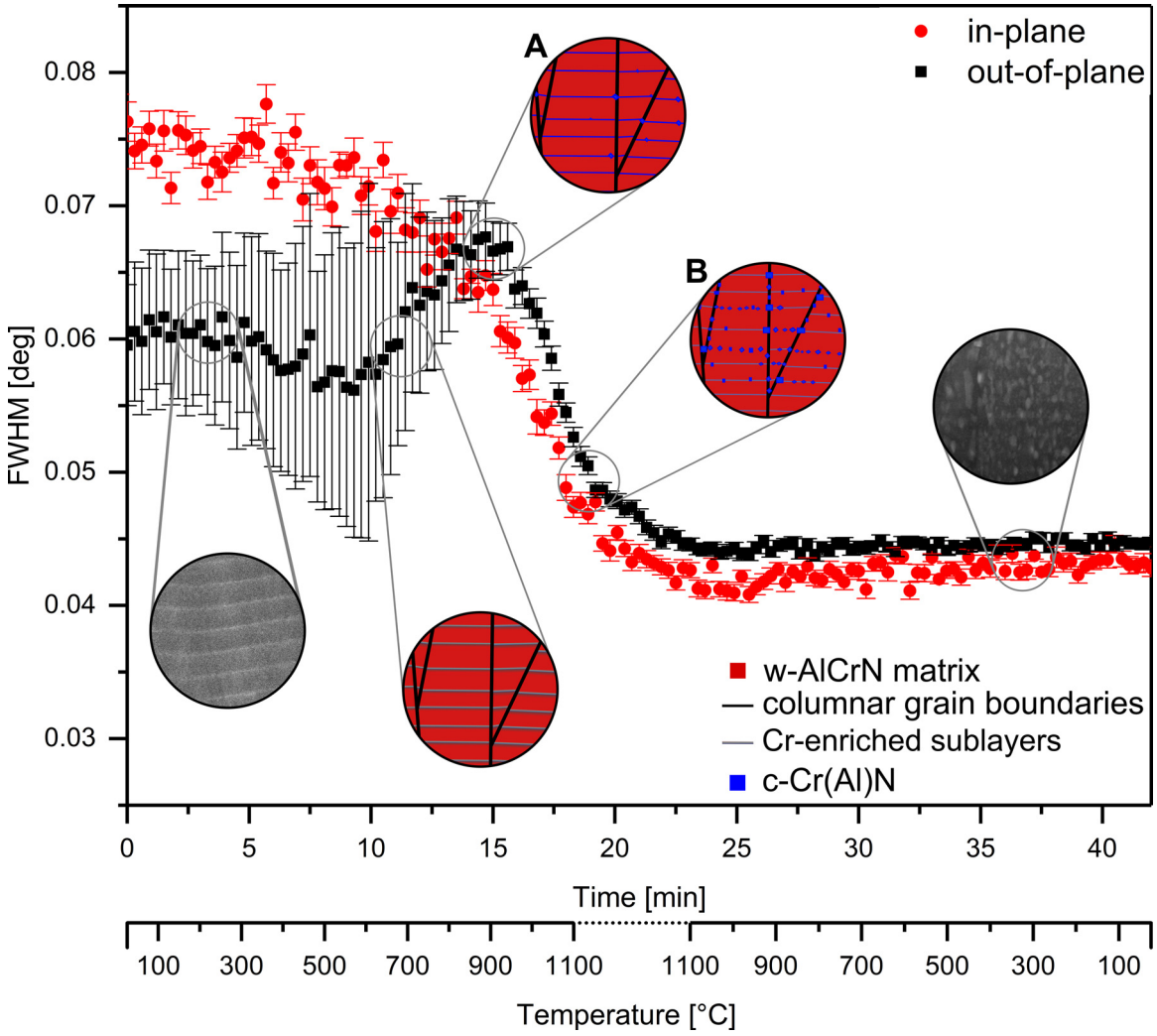

Fig. 10. Temperature evolution of in-plane and out-of-plane FWHMs of the h-100 reflection for in-plane and out-of-plane diffraction vector orientation, respectively. The inserts show schematically the microstructural changes relevant for the out-of-plane FWHM evolution, namely Cr segregation (A) at the sublayer interfaces and the subsequent formation of precipitates (B) during the heat treatment, in agreement with the TEM data from Figs. 4–6. The stepwise FWHM decrease in the range of 900-1100°C (for both diffraction vector orientations) is related to microstructure recovery and defect annihilation.

ported on an epitaxial relationship in the case of the AlN-CrN interface [70], namely w-AlCrN(0001)[11-20]||c-Cr(Al)N(111)[011]. On the basis of this epitaxial relationship, interface surface energies of 3.9 and 2.7 J/m^2 were calculated for w-AlN/c-AlN and w-AlN/c-CrN interfaces. Apparently, the range of γ values for such interface is larger than the minimum surface energy of w-AlN ($\gamma_{(1\text{-}100)} = 2.3\,\text{J/m}^2$) and therefore is again not expected to be a limiting factor of the fracture strength after the annealing.

Since the c-Cr(Al)N particles precipitate (also) at the grain boundaries, the crack propagating along such decorated grain boundary and eventually hitting the cubic precipitate will choose to continue along the path corresponding to the lowest cleavage energy. From the above analysis this is through w-AlCrN grains, hence yielding to trans-granular fracture. When such particles are not present in the as-deposited state, the crack is expected to propagate along the grain boundaries, thus leading to inter-granular fracture. Based on those qualitative arguments we therefore propose that the observed increase in the film's toughness, represented by the slight increase in fracture toughness and the decrease of the critical flaw size, is primarily caused by the precipitation at the grain-boundaries. The formed precipitates (c-Cr(Al)N) are tougher than the matrix phase (w-AlCrN) and form tough interfaces to the matrix via a well-defined epitaxial relationship. Since there is common agreement also in the experimental data [51,59], that the c-Cr(Al)N phase is harder and stiffer compared to the w-AlCrN phase, this leaves only the weaker fracture path through the matrix grains.

4. Discussion

4.1. Film microstructure

The initial w-$Al_{0.9}Cr_{0.1}N$ film microstructure comprised grain boundaries between the columnar grains and Cr-enriched sublayers within the grains, which both represent trap sites for the segregation of Cr and the subsequent formation of c-Cr(Al)N precipitates (Figs. 1, 4–6). Generally, the chemical variations along the cross-section without interrupting the growth of columnar grains is a typical feature of films deposited by cathodic arc evaporation. The cross-sectional variation of the Cr content can be explained by a combination of (i) the angular anisotropic evaporation kinetics of Al and Cr and (ii) the rotation of the substrate carousel within the

deposition chamber, as found for TiSiC, TiSiCN, TiAlON and TiAlN thin films [43–48]. These lead to a periodical excitation of the Cr content to ∼16% at the metal sublattice (*cf*. Figs. 4a,c and 7), substantially closer to the formation of the c-Cr(Al)N phase compared to the matrix (*cf*. Table 1), with a cross-sectional periodicity of ∼34 nm (Figs. 5 and 7). These periodic chemical fluctuations embedded in the columnar grains result in short diffusion paths for segregation and represent thus a reservoir for the precipitation during the heat treatment.

Upon the annealing, the overall columnar-grained morphology of the film did not change, as can be seen by SEM and TEM micrographs (Figs. 1, 4–6). However, in detail, the formation of c-Cr(Al)N and c-CrN precipitates at the intracrystalline (formerly Cr-enriched) sublayers' interfaces as well as at the columnar grain boundaries took place during the heat treatment. No pores formed during the heat treatment were found, in contrast to the TiN presented in Ref. [10]. The c-Cr(Al)N precipitates at the sublayers' interfaces (and therefore in the grain interior) are smaller compared to the c-CrN precipitates at the grain boundaries. Both the differences in the composition and the size can be attributed to the limited diffusion within the grains (*i.e*. bulk diffusion is slower compared to grain boundary diffusion [71]). While the formation of a secondary c-ZrN phase at the grain boundary of w-ZrAlN was already reported in literature [15], the formation of the inherently metastable c-Cr(Al)N within the grains is unprecedented. A somewhat similar grain interior was up to now only reported from decomposed lamellar CVD TiAlN thin films [72,73], where c-TiN grains were embedded in a w-AlN matrix, however, c-TiN is a stable decomposition product of TiAlN. Long-term annealing of plasma-sprayed thermal barrier coatings leads to inter-column bonding, so called sintering, and consequently increased Young's modulus and fracture strength [74–77]. Although sintering is performed in a similar temperature range (1100°C–1400°C) compared with the heat treatment presented in this work, the time ranges (5-500h) are at least two orders of magnitude higher [74–77]. Furthermore, a significant porosity is a prerequisite for sintering [74–77], concurring with the microstructure of the here investigated film (Fig. 1a,c, Suppl. Fig. 1a). Additionally, the consumption of the pores during sintering leads furthermore to a shrinkage, whereas the here presented film's thickness after annealing remains constant (Fig. 1, Suppl. Fig. 1). Therefore, one can conclude, that the concomitant increase of Young's modulus, fracture stress and fracture toughness presented in Section 3.2 and discussed in Section 4.3. can be attributed to the intra- and intercolumnar precipitation confirmed by SEM (Fig. 1), TEM (Figs. 4 and 6) and APT (Fig. 8).

4.2. High-temperature behavior of w-AlCrN films

Contrary to the c-Cr(Al)N with Al content of less than ∼70%, which was studied extensively in the past [51], only little attention was drawn to the high-temperature behavior of w-$Al_{0.9}Cr_{0.1}N$. This wurtzite phase is in general considered as non-desirable in metastable transition metal nitrides due to its rather poor mechanical properties compared to c-Cr(Al)N or c-TiAlN [51,78], despite its superior thermal stability and oxidation resistance [22,79]. The reported decomposition pathway of w-AlCrN includes in general the formation of c-CrN precipitates and the decomposition of c-CrN into h-Cr_2N and Cr when reaching temperatures above 950, 1250 and 1300°C, respectively [80]. Given the results from Figs. 1, and 4–8, this decomposition pathway has to be amended for arc-evaporated thin films and the formation of c-Cr(Al)N within the grain interior has to be added. The evolution of crystalline phases in the HE-HT-GIT XRD phase plot (Fig. 9) shows no pronounced phase changes in the temperature range of 25-1100°C, however the absence of the c-CrN-related signal is related to the experimental conditions depicted in Sections 2 and 3. These findings are also confirmed by the films' cross-sections before and after the heat-treatment shown in Fig. 1, where only nanoscopic changes in the microstructure after the annealing could be detected.

Generally, the texture of w-AlCrN thin films is usually very sensitive to the applied bias voltage, where changes in the typical range of 0 to -150 V lead to a switching from a ⟨002⟩ to a mixture of ⟨100⟩ and ⟨110⟩ fibre textures [55,56,81], respectively. The latter is consistent with the present results and furthermore did not change during the heat-treatment (*cf*. Suppl. Fig. 5).

Simultaneously, with the increasing bias voltage, the AlN lattice constant a increases [82,83], while c_0 remains rather unaffected. This behavior is even more pronounced by the addition of Cr, which is mainly incorporated in the crystallites' basal planes, thus further increasing the a-axis length [61]. Consequently, in the crystallites with ⟨100⟩ and ⟨110⟩ fibre textures, the {001} planes are oriented perpendicular to the interfaces between the sublayers and consequently the Cr diffusion proceeds along the crystallites' a-axes. Altogether, up to this point, the high-temperature evolution of the w-AlCrN film is in agreement to prior reported results [61,80], but gives new insights into the distribution of Cr in the wurtzite crystal structure and diffusion of Cr out of the lattice.

A significant insight into the microstructural changes within the columnar grains was obtained from the FWHM analysis presented in Fig. 10, which will be discussed only qualitatively. For the in-plane orientation of the diffraction vectors, the steep decrease in the FWHM of the w-AlCrN 100 reflections can be related to the microstructure recovery and the annihilation of the defects during annealing above the deposition temperature of 475°C. Other parameters like the in-plane width of the columnar grains did not change during annealing (*cf*. Figs. 1, 4–6) and furthermore the c-Cr(Al)N precipitates grew mainly at the columnar grain boundaries and the sublayers' interfaces oriented parallel to the in-plane direction. Contrary, the FWHM of the w-AlCrN 100 reflections evaluated for the out-of-plane diffraction vector orientation is dominated (i) by the changes in the defect density above 475°C (like for the in-plane orientation) and (ii) by the c-Cr(Al)N precipitate formation along the interfaces between the sublayers, which naturally reduce the size of the coherently diffracting domains. Above the deposition temperature, the out-of-plane FWHM increased up to a temperature of 950°C, contrary to the ongoing defect annihilation found for the in-plane orientation (Fig. 10). This effect can be related to the Cr segregation along the interfaces of the sublayers and the formation of incoherent interfaces. Up to ∼950°C the Cr content along the layer boundaries gradually increases, which results in the formation of a segregated layer of presumably coherent c-CrN. Above 950 up to 1100°C, the defect annihilation became dominant and resulted in the stepwise decrease of the out-of-plane FWHM.

No significant recovery or precipitate formation took place below the deposition temperature of 475°C, which indicates insufficient driving force delivered to the system at low temperatures to activate diffusion-driven processes. The decrease of the in-plane and out-of-plane FWHMs above the deposition temperature and ∼800°C, respectively, can be nicely correlated with the compressive residual stress relaxation (Fig. 9d) from ∼-5.1 ± 0.1 to -0.9 ± 0.1 GPa caused by the microstructure recovery. The ongoing defect annihilation during the holding segment is also reflected by the further (nearly exponential) decrease of the in-plane FWHM (Fig. 10) and in-plane residual stress (Fig. 9d). During cooling down, no further changes in FWHM were observed, reflecting a rather constant defect density, whereas the residual stress gradually increased as a consequence of CTE mismatch between the substrate and the film [21].

4.3. Changes in fracture behavior

Nanocrystalline ceramic thin films preferentially fracture in a brittle manner usually along columnar grain boundaries of low cohesive energy. Beside the known textbook phenomena for macroscopic ceramics, such as crack tip shielding and crack-wake bridging [32], there are several strategies based on state-of-the art thin film technology to overcome the detrimental brittle fracture at grain boundaries of low cohesive energy. Typically, alloying of the thin films was designed to improve stiffness and strength of the matrix, and segregation of secondary phases and decomposition of the matrix should be retarded to as high temperatures as possible [21,56]. Additionally, multi-layered thin films were designed to decelerate the propagating crack and improve fracture toughness [5,6]. Similar, sculptured thin films were designed to increase fracture toughness [2,84]. Therefore, most approaches focussed on the increase of the number of interfaces along the expected crack path, which results in an increased number of crack deflection events, in energy dissipation and finally in the improvement of mechanical properties, *cf.* for example [5,6,85,86].

On the other hand, up to now, there is no study, which would show a possibility to purposefully alter grain boundaries of TMN thin films to prevent fracture along the columnar grain boundaries of low cohesive energy. However, in bulk metallic alloys, grain boundary segregation of secondary elements is frequently used to enhance fracture resistance. Best examples are high-Mn containing steels [17,87,88], Al-alloys [89] or B-doped Mo [18–20], a concept which was here transferred to w-AlCrN based thin films.

In the present work, the measured increase in the *film's fracture stress* of 65% from 3.2 to 5.1 GPa (*cf.* Table 3) via grain boundary segregation engineering is not completely reflected by the *hardness* increase of 33% from 18.3 to 24.3 GPa (*cf.* Table 2), which can be associated with a relatively high equibiaxial residual stress state of ∼-5.1 ± 0.1 GPa in the as-deposited film (*cf.* Fig. 9d). When accounting for the change in the residual stress state from -5.1 ± 0.1 to -1.1 ± 0.1 GPa after the annealing in the respective films, it can be recognized that the increase in the film's hardness of ∼76% (from ∼13 to ∼23 GPa) is coincidently comparable to the observed change in the fracture stress of 65% revealed by the microcantilever bending tests (*cf.* Tables 2 and 3). Comparable micromechanical studies on annealed TMN thin films indicate usually a deterioration of the mechanical properties after annealing. Exemplary, for PVD CrN [9], an as-deposited fracture stress of ∼5.9 GPa was measured, which after the annealing to 500°C was reduced to ∼4.4 GPa due to defect annihilation at the grain boundaries, which negatively affected the cohesive strength. Similar, mechanical properties of TiN based deteriorate already at annealing temperatures of ∼500°C [10], similar to CrN [9].

The measured *fracture toughness* of 2.7 MPa m^{½} (Table 3) of the w-AlCrN film in as-deposited state is not exceptional, yet significantly exceeds for example reported values for TiN (1.2 MPa m^{½}) [5], modulus-matched cubic $Al_{0.6}Cr_{0.4}N$/TiN superlattices (2.5 MPa m^{½}) [90], TaC (1.8 MPa m^{½}) [91] or HfCN (<2.3 MPa m^{½}) [92]. All these studies on TMN films indicate an intergranular fracture and this appears to be the case also for the superlattice TiN/WN (4.7 MPa m^{½}) and Cr/CrN (5.0 MPa m^{½}) multilayer films (*in the as-deposited state*) with highest reported fracture toughness values in the field of PVD TMN films [5,7]. Contrary to advanced multi-scale interface design of PVD films, where higher fracture toughness is achieved by elastic interlayers interrupting the stiff matrix [8], in this study strengthening is achieved by hard precipitates blocking the fracture path at the grain boundaries and forcing crack growth in the w-Al(Cr)N matrix. Similarly to the fracture strength discussed above, the comparative studies on the fracture toughness of CrN [9] (3.8 MPa m^{½}) and TiN [10] (2.9 MPa m^{½}) in as-deposited state exceed fracture toughness of the here presented w-AlCrN (2.7 MPa m^{½}), *cf.* Table 3. Yet after an annealing to 500°C the fracture toughness of comparative CrN and TiN decreases to 3.05 and 2.5 MPa m^{½} (*cf.* Refs. [9] and [10]), respectively, while grain boundary segregation in the present w-AlCrN at 1100°C leads to an increase of fracture toughness to 3.0 MPa m^{½}. For both CrN [9] and TiN [10], the deterioration of fracture toughness after the annealing was attributed to defect annihilation at the grain boundaries, additionally, for TiN the formation of pores at the grain boundaries was detected. In the case of metastable TiAlN, which showed a pronounced hardening by an annealing [78], the fracture toughness increased from 2.7 in as-deposited state to 3.0 MPa m^{½} and after the annealing at 900°C, followed by a decrease to 2.7 MPa m^{½} due to the formation of the secondary w-Al(Ti)N, when increasing the annealing temperature to 1000°C [4], all without changing the fracture mode of the cantilevers.

Beside the fact, that the application of the Griffith crack criterion (Eq. (6)) is only valid in continuum mechanics [32], it can be helpful in the interpretation of the fracture toughness increase. Given an ideal dense-free continuum solid, the fracture toughness is proportional to the square root of the Young's modulus ($K_{IC} \propto \sqrt{E}$), an increase of the experimentally determined modulus by ∼31–47% (*cf.* Table 3) is expected to result in the increase of fracture toughness by 14–21%, while experimentally only an increase of 10–11% was evaluated. Consequently, this mismatch could be interpreted by changes in the surface energy (*cf.* Eq. (6)), possibly related to the change from inter- to transcrystalline fracture after annealing and a diminished cantilevers fracture surface roughness as indicated by Fig. 3. Additionally, the actual change of fracture toughness may be hidden in the relatively high experimental scatter, which may be reduced by the application of neural networks [93,94] in future works. In summary, by applying the dedicated annealing treatment, it was possible to improve the Young's modulus of the metastable nanoceramic w-AlCrN thin film by ∼31–47%, the fracture stress by 37–59% and simultaneously K_{IC} by 10–11%. Finally, it can be expected, that the results obtained in this study will trigger a development of novel nanocrystalline ceramics thin films with high hardness and toughness based on precipitation-based grain boundary design.

5. Conclusions

Carefully adjusted thermal processing of arc-evaporated thin films resulted into precipitate formation and concomitant strengthening of both the grain interior and grain boundaries of a w-$Al_{0.9}Cr_{0.1}N$ thin film. The precipitations could be identified as globular c-Cr(Al)N and elongated c-CrN within the grains and at the grain boundaries with sizes ranging to ∼<10 and ∼25 nm, respectively. Once the precipitates formed the fracture morphology from inter-columnar to trans-columnar fracture, accompanied by a simultaneous increase of Young's modulus, fracture strength and fracture toughness from 212 ± 18 to 311 ± 18 GPa, 3.2 ± 0.4 to 5.1 ± 0.4 GPa and 2.7 ± 0.3 to 3.0 ± 0.2 MPa m^{½}, respectively. These trends were qualitatively confirmed by *ab initio based tensile strength* calculations. The here reported experimental and theoretical data uncovers the previously overlooked potential of precipitation-based grain boundary design for transition metal nitride thin films with improved mechanical behavior. In general, the present work introduces a precipitation-based grain boundary design as an effective design guideline to alter usually observed intergranular fracture of brittle nanocrystalline thin films. The precipitation of elongated c-CrN precipitates at at columnar grain boundaries is used as a novel strategy to improve the mechanical properties of the grain boundaries and to initiate transgranular crack growth across the loaded films, which in turn result in the enhanced overall mechanical properties.

Declaration of Competing Interest

The authors declare that they have no known competing financial interests or personal relationships that could have appeared to influence the work reported in this paper.

Acknowledgment

The work has been financially supported by Christian Doppler Research Association. The financial support by the Austrian Federal Ministry for Digital and Economic Affairs and the National Foundation for Research, Technology and Development is gratefully acknowledged. The CzechNanoLab project LM2018110 funded by MEYS CR is gratefully acknowledged for the financial support of the measurements/sample fabrication at CEITEC Nano Research Infrastructure. DH and LL acknowledge financial support from Austrian Science Fund (P30341-N36). The computational results presented have been achieved using the Vienna Scientific Cluster (VSC).

Supplementary materials

Supplementary material associated with this article can be found, in the online version, at doi:10.1016/j.actamat.2022.118156.

References

[1] A.G. Evans, Perspective on the development of high-toughness ceramics, J. Am. Ceram. Soc. 73 (1990) 187–206, doi:10.1111/j.1151-2916.1990.tb06493.x.
[2] R. Daniel, M. Meindlhumer, W. Baumegger, J. Zalesak, B. Sartory, M. Burghammer, C. Mitterer, J. Keckes, Grain boundary design of thin films: Using tilted brittle interfaces for multiple crack deflection toughening, Acta Mater. 122 (2017) 130–137, doi:10.1016/j.actamat.2016.09.027.
[3] W.M. Seidl, M. Bartosik, S. Kolozsvári, H. Bolvardi, P.H. Mayrhofer, Influence of Ta on the fracture toughness of arc evaporated Ti-Al-N, Vacuum 150 (2018) 24–28, doi:10.1016/j.vacuum.2018.01.028.
[4] M. Bartosik, C. Rumeau, R. Hahn, Z.L. Zhang, P.H. Mayrhofer, Fracture toughness and structural evolution in the TiAlN system upon annealing, Sci. Rep. 7 (2017) 1–9, doi:10.1038/s41598-017-16751-1.
[5] R. Daniel, M. Meindlhumer, J. Zalesak, B. Sartory, A. Zeilinger, C. Mitterer, J. Keckes, Fracture toughness enhancement of brittle nanostructured materials by spatial heterogeneity: A micromechanical proof for CrN/Cr and TiN/SiOx multilayers, Mater. Des. 104 (2016) 227–234, doi:10.1016/j.matdes.2016.05.029.
[6] R. Hahn, M. Bartosik, R. Soler, C. Kirchlechner, G. Dehm, P.H. Mayrhofer, Superlattice effect for enhanced fracture toughness of hard coatings, Scr. Mater. 124 (2016) 67–70, doi:10.1016/j.scriptamat.2016.06.030.
[7] J. Buchinger, N. Koutná, Z. Chen, Z. Zhang, P.H. Mayrhofer, D. Holec, M. Bartosik, Toughness enhancement in TiN/WN superlattice thin films, Acta Mater. 172 (2019) 18–29, doi:10.1016/j.actamat.2019.04.028.
[8] R. Daniel, M. Meindlhumer, J. Zalesak, W. Baumegger, J. Todt, T. Ziegelwanger, J.F. Keckes, C. Mitterer, J. Keckes, Multi-scale interface design of strong and damage resistant hierarchical nanostructured materials, Mater. Des. 196 (2020) 109169, doi:10.1016/j.matdes.2020.109169.
[9] A. Riedl, R. Daniel, M. Stefenelli, T. Schöberl, O. Kolednik, C. Mitterer, J. Keckes, A novel approach for determining fracture toughness of hard coatings on the micrometer scale, Scr. Mater. 67 (2012) 708–711, doi:10.1016/j.scriptamat.2012.06.034.
[10] J. Buchinger, L. Löfler, J. Ast, A. Wagner, Z. Chen, J. Michler, Z.L. Zhang, P.H. Mayrhofer, D. Holec, M. Bartosik, Fracture properties of thin film TiN at elevated temperatures, Mater. Des. 194 (2020) 1–10, doi:10.1016/j.matdes.2020.108885.
[11] H. Köstenbauer, G.A. Fontalvo, M. Kapp, J. Keckes, C. Mitterer, Annealing of intrinsic stresses in sputtered TiN films: the role of thickness-dependent gradients of point defect density, Surf. Coat. Technol. 201 (2007) 4777–4780, doi:10.1016/j.surfcoat.2006.10.017.
[12] A. Drnovsek, H.T. Vo, M. Rebelo De Figueiredo, S. Kolozsvari, P. Hosemann, R. Franz, High temperature fracture toughness of single-layer CrAlN and CrAlSiN hard coatings, Surf. Coat. Technol. 409 (2021), doi:10.1016/j.surfcoat.2021.126909.
[13] L. Hultman, C. Engström, M. Odén, Mechanical and thermal stability of TiN/NbN superlattice thin films, Surf. Coat. Technol. 133–134 (2000) 227–233, doi:10.1016/S0257-8972(00)00935-X.
[14] C. Engström, J. Birch, L. Hultman, C. Lavoie, C. Cabral, J.L. Jordan-Sweet, J.R.A. Carlsson, Interdiffusion studies of single crystal TiN/NbN superlattice thin films, J. Vac. Sci. Technol. A Vac. Surf. Film 17 (1999) 2920–2927, doi:10.1116/1.581961.
[15] L. Rogström, N. Ghafoor, J. Schroeder, N. Schell, J. Birch, M. Ahlgren, M. Odén, Thermal stability of wurtzite Zr1-xAlxN coatings studied by *in situ* high-energy x-ray diffraction during annealing, J. Appl. Phys. 118 (2015) 9, doi:10.1063/1.4927156.
[16] D. Raabe, M. Herbig, S. Sandlöbes, Y. Li, D. Tytko, M. Kuzmina, D. Ponge, P.P. Choi, Grain boundary segregation engineering in metallic alloys: a pathway to the design of interfaces, Curr. Opin. Solid State Mater. Sci. 18 (2014) 253–261, doi:10.1016/j.cossms.2014.06.002.
[17] D. Raabe, S. Sandlöbes, J. Millán, D. Ponge, H. Assadi, M. Herbig, P.P. Choi, Segregation engineering enables nanoscale martensite to austenite phase transformation at grain boundaries: A pathway to ductile martensite, Acta Mater. 61 (2013) 6132–6152, doi:10.1016/j.actamat.2013.06.055.
[18] S. Jakob, A. Hohenwarter, A. Lorich, W. Knabl, R. Pippan, H. Clemens, V. Maier-Kiener, Assessment of grain boundary cohesion of technically pure and boron micro-doped molybdenum via meso-scale three-point-bending experiments, Mater. Des. 207 (2021) 109848, doi:10.1016/j.matdes.2021.109848.
[19] K. Leitner, D. Lutz, W. Knabl, M. Eidenberger-Schober, K. Huber, A. Lorich, H. Clemens, V. Maier-Kiener, Grain boundary segregation engineering in as-sintered molybdenum for improved ductility, Scr. Mater. 156 (2018) 60–63 (née Babinsky), doi:10.1016/j.scriptamat.2018.07.008.
[20] K. Leitner, P.J. Felfer, D. Holec, J. Cairney, W. Knabl, A. Lorich, H. Clemens, S. Primig, On grain boundary segregation in molybdenum materials, Mater. Des. 135 (2017) 204–212 (née Babinsky), doi:10.1016/j.matdes.2017.09.019.
[21] M. Meindlhumer, S. Klima, N. Jäger, A. Stark, H. Hruby, C. Mitterer, J. Keckes, R. Daniel, Stress-controlled decomposition routes in cubic AlCrN films assessed by *in-situ* high-temperature high-energy grazing incidence transmission X-ray diffraction, Sci. Rep. 9 (2019) 1–14, doi:10.1038/s41598-019-54307-7.
[22] J. Todt, R. Pitonak, A. Köpf, R. Weißenbacher, B. Sartory, M. Burghammer, R. Daniel, T. Schöberl, J. Keckes, Superior oxidation resistance, mechanical properties and residual stresses of an Al-rich nanolamellar Ti0.05Al0.95N coating prepared by CVD, Surf. Coat. Technol. 258 (2014) 1119–1127, doi:10.1016/j.surfcoat.2014.07.022.
[23] N. Jäger, M. Meindlhumer, S. Spor, H. Hruby, J. Julin, A. Stark, F. Nahif, J. Keckes, C. Mitterer, R. Daniel, Microstructural evolution and thermal stability of AlCr(Si)N hard coatings revealed by *in-situ* high-temperature high-energy grazing incidence transmission X-ray diffraction, Acta Mater. 186 (2020) 545–554, doi:10.1016/j.actamat.2020.01.026.
[24] N. Jäger, M. Meindlhumer, M. Zitek, S. Spor, H. Hruby, F. Nahif, J. Julin, J. Keckes, C. Mitterer, R. Daniel, Impact of Si on the high-temperature oxidation of AlCr(Si)N coatings, J. Mater. Sci. Technol. 100 (2021) 91–100, doi:10.1016/j.jmst.2021.04.065.
[25] M. Klinger, More features, more tools, more CrysTBox, J. Appl. Crystallogr. 50 (2017) 1226–1234, doi:10.1107/S1600576717006793.
[26] M. Hans, J.M. Schneider, On the chemical composition of TiAlN thin films - Comparison of ion beam analysis and laser-assisted atom probe tomography with varying laser pulse energy, Thin Solid Films 688 (2019) 137251, doi:10.1016/j.tsf.2019.04.026.
[27] M. Hans, J.M. Schneider, Electric field strength-dependent accuracy of TiAlN thin film composition measurements by laser-assisted atom probe tomography, New J. Phys. 22 (2020), doi:10.1088/1367-2630/ab7770.
[28] K. Thompson, D. Lawrence, D.J. Larson, J.D. Olson, T.F. Kelly, B. Gorman, *In situ* site-specific specimen preparation for atom probe tomography, Ultramicroscopy 107 (2007) 131–139, doi:10.1016/j.ultramic.2006.06.008.
[29] B.N. Jaya, C. Kirchlechner, G. Dehm, Can microscale fracture tests provide reliable fracture toughness values? A case study in silicon, J. Mater. Res. 30 (2015) 686–698, doi:10.1557/jmr.2015.2.
[30] J.P. Best, J. Zechner, J.M. Wheeler, R. Schoeppner, M. Morstein, J. Michler, Small-scale fracture toughness of ceramic thin films: the effects of specimen geometry, ion beam notching and high temperature on chromium nitride toughness evaluation, Philos. Mag. 96 (2016) 3552–3569, doi:10.1080/14786435.2016.1223891.
[31] H. Tada, P.C. Paris, G.R. Irwin, The Stress Analysis of Cracks Handbook, 3rd ed., ASME, New York, 2000.
[32] B.R. Lawn, Fracture of Brittle Solids, 2nd ed., Cambridge University Press, Cambridge CB2 1RP, 1993.
[33] G. Kresse, J. Furthmüller, Efficient iterative schemes for ab initio total-energy calculations using a plane-wave basis set, Phys. Rev. B 54 (1996) 169–185, doi:10.1021/acs.jpca.0c01375.
[34] G. Kresse, J. Furthmüller, Efficiency of *ab-initio* total energy calculations for metals and semiconductors using a plane-wave basis set, Comput. Mater. Sci. 6 (1996) 15–50, doi:10.1016/0927-0256(96)00008-0.
[35] J.P. Perdew, K. Burke, M. Ernzerhof, Generalized gradient approximation made simple, Phys. Rev. Lett. 77 (1996) 3865–3868, doi:10.1103/PhysRevLett.77.3865.
[36] G. Kresse, D. Joubert, From ultrasoft pseudopotentials to the projector augmented-wave method, Phys. Rev. B Condens. Matter Mater. Phys. 59 (1999) 1758–1775, doi:10.1103/PhysRevB.59.1758.
[37] H.J. Monkhorst, J.D. Pack, Special points for Brillouin-zone integrations, Phys. Rev. B 13 (1976) 5188–5192, doi:10.1103/PhysRevB.16.1748.
[38] L.M. Corliss, N. Elliott, J.M. Hastings, Antiferromagnetic structure of CrN, Phys. Rev. 117 (1960) 929–935, doi:10.1103/PhysRev.117.929.
[39] P. Lazar, J. Redinger, J. Strobl, R. Podloucky, B. Rashkova, G. Dehm, G. Kothleitner, S. Šturm, K. Kutschej, C. Mitterer, C. Scheu, N-K electron energy-loss near-edge structures for TiN/VN layers: An ab initio and experimental study, Anal. Bioanal. Chem. 390 (2008) 1447–1453, doi:10.1007/s00216-007-1759-0.

[40] A. Hörling, L. Hultman, M. Odén, J. Sjölén, L. Karlsson, Thermal stability of arc evaporated high aluminum-content Ti1−xAlxN thin films, J. Vac. Sci. Technol. A Vac. Surf. Film. 20 (2002) 1815–1823, doi:10.1116/1.1503784.

[41] M. Pohler, R. Franz, J. Ramm, P. Polcik, C. Mitterer, Cathodic arc deposition of $(Al,Cr)_2O_3$: macroparticles and cathode surface modifications, Surf. Coat. Technol. 206 (2011) 1454–1460, doi:10.1016/j.surfcoat.2011.09.028.

[42] P. Panjan, A. Drnovšek, P. Gselman, M. Čekada, M. Panjan, Review of growth defects in thin films prepared by PVD techniques, 2020. 10.3390/COATINGS10050447.

[43] A.O. Eriksson, J.Q. Zhu, N. Ghafoor, M.P. Johansson, J. Sjölen, J. Jensen, M. Odén, L. Hultman, J. Rosén, Layer formation by resputtering in Ti-Si-C hard coatings during large scale cathodic arc deposition, Surf. Coat. Technol. 205 (2011) 3923–3930, doi:10.1016/j.surfcoat.2011.02.007.

[44] A.O. Eriksson, J. Zhu, N. Ghafoor, J. Jensen, G. Greczynski, M.P. Johansson, J. Sjölen, M. Odén, L. Hultman, J. Rosén, Ti-Si-C-N thin films grown by reactive arc evaporation from Ti_3SiC_2 cathodes, J. Mater. Res. 26 (2011) 874–881, doi:10.1557/jmr.2011.10.

[45] A. Khatibi, J. Sjölen, G. Greczynski, J. Jensen, P. Eklund, L. Hultman, Structural and mechanical properties of Cr-Al-O-N thin films grown by cathodic arc deposition, Acta Mater. 60 (2012) 6494–6507, doi:10.1016/j.actamat.2012.08.010.

[46] M. Hans, M. to Baben, Y.T. Chen, K.G. Pradeep, D.M. Holzapfel, D. Primetzhofer, D. Kurapov, J. Ramm, M. Arndt, H. Rudigier, J.M. Schneider, Substrate rotation-induced chemical modulation in Ti-Al-O-N coatings synthesized by cathodic arc in an industrial deposition plant, Surf. Coat. Technol. 305 (2016) 249–253, doi:10.1016/j.surfcoat.2016.08.046.

[47] S. Gleich, R. Soler, H. Fager, H. Bolvardi, J.O. Achenbach, M. Hans, D. Primetzhofer, J.M. Schneider, G. Dehm, C. Scheu, Modifying the nanostructure and the mechanical properties of Mo2BC hard coatings: Influence of substrate temperature during magnetron sputtering, Mater. Des. 142 (2018) 203–211, doi:10.1016/j.matdes.2018.01.029.

[48] D.M. Holzapfel, D. Music, M. Hans, S. Wolff-Goodrich, D. Holec, D. Bogdanovski, M. Arndt, A.O. Eriksson, K. Yalamanchili, D. Primetzhofer, C.H. Liebscher, J.M. Schneider, Enhanced thermal stability of (Ti,Al)N coatings by oxygen incorporation, Acta Mater. 218 (2021) 117204, doi:10.1016/j.actamat.2021.117204.

[49] V. Edlmayr, M. Pohler, I. Letofsky-Papst, C. Mitterer, Microstructure and thermal stability of corundum-type $(Al_{0.5}Cr_{0.5})_2O_3$ solid solution coatings grown by cathodic arc evaporation, Thin Solid Films 534 (2013) 373–379, doi:10.1016/j.tsf.2013.02.046.

[50] A. Hörling, L. Hultman, M. Odén, J. Sjölén, L. Karlsson, Mechanical properties and machining performance of Ti1-xAlxN-coated cutting tools, Surf. Coat. Technol. 191 (2005) 384–392, doi:10.1016/j.surfcoat.2004.04.056.

[51] A.E. Reiter, V.H. Derflinger, B. Hanselmann, T. Bachmann, B. Sartory, Investigation of the properties of $Al_{1-x}Cr_xN$ coatings prepared by cathodic arc evaporation, Surf. Coat. Technol. 200 (2005) 2114–2122, doi:10.1016/j.surfcoat.2005.01.043.

[52] V. Moraes, H. Riedl, R. Rachbauer, S. Kolozsvári, M. Ikeda, L. Prochaska, S. Paschen, P.H. Mayrhofer, Thermal conductivity and mechanical properties of AlN-based thin films, J. Appl. Phys. 119 (2016), doi:10.1063/1.4953358.

[53] B.S. Li, T.J. Marrow, S.G. Roberts, D.E.J. Armstrong, Evaluation of fracture toughness measurements using Chevron-Notched silicon and tungsten microcantilevers, JOM 71 (2019) 3378–3389, doi:10.1007/s11837-019-03696-1.

[54] A. Naughton-Duszová, T. Csanádi, R. Sedlák, P. Hvizdoš, J. Dusza, Small-scale mechanical testing of cemented carbides from the micro- to the nano-level: a review, Metals 9 (2019) 1–26 (Basel), doi:10.3390/met9050502.

[55] S. Klima, N. Jäger, H. Hruby, C. Mitterer, J.F. Keckes, M. Burghammer, R. Daniel, Structure-stress relationships in nanocrystalline multilayered Al 0.7 Cr 0.3 N/Al 0.9 Cr 0.1 N coatings studied by cross-sectional X-ray nanodiffraction, Mater. Des. 170 (2019) 107702, doi:10.1016/j.matdes.2019.107702.

[56] N. Jäger, S. Klima, H. Hruby, J. Julin, M. Burghammer, J.F. Keckes, C. Mitterer, R. Daniel, Evolution of structure and residual stress of a fcc/hex-AlCrN multi-layered system upon thermal loading revealed by cross-sectional X-ray nano-diffraction, Acta Mater. 162 (2019) 55–66, doi:10.1016/j.actamat.2018.09.031.

[57] B. Gault, D.W. Saxey, M.W. Ashton, S.B. Sinnott, A.N. Chiaramonti, M.P. Moody, D.K. Schreiber, Behavior of molecules and molecular ions near a field emitter, New J. Phys. 18 (2016) 33031, doi:10.1088/1367-2630/18/3/033031.

[58] S. Jin Rotert, D. Music, M. To Baben, J.M. Schneider, Theoretical study of elastic properties and phase stability of $M_{0.5}Al_{0.5}N_{1-x}O_x$ (M = Sc, Ti, V, Cr), J. Appl. Phys. 113 (2013) 0–4, doi:10.1063/1.4793496.

[59] M. Kawate, A. Kimura, T. Suzuki, Microhardness and lattice parameter of $Cr_{1-x}Al_xN$ films, J. Vac. Sci. Technol. A Vac. Surf. Film. 20 (2002) 569–571, doi:10.1116/1.1448510.

[60] Powder Diffraction File Cards: w-AlN 225–1133, WC 25-1047, Co 15-0806, (n.d.) accessed January 2022

[61] P.H. Mayrhofer, D. Music, T. Reeswinkel, H.G. Fuß, J.M. Schneider, Structure, elastic properties and phase stability of $Cr_{1-x}Al_xN$, Acta Mater. 56 (2008) 2469–2475, doi:10.1016/j.actamat.2008.01.054.

[62] P. Hidnert, Thermal expansion of cemented tungsten carbide, J. Res. Natl. Bur. Stand. 18 (1934) 47 1937, doi:10.6028/jres.018.025.

[63] M. Birkholz, Thin Film Analysis by X-ray Scattering, Wiley-VCH Verlag GmbH & Co, KGaA, Weinheim, 2006.

[64] R. Hahn, N. Koutná, T. Wójcik, A. Davydok, S. Kolozsvári, C. Krywka, D. Holec, M. Bartosik, P.H. Mayrhofer, Mechanistic study of superlattice-enabled high toughness and hardness in MoN/TaN coatings, Commun. Mater. 1 (2020), doi:10.1038/s43246-020-00064-4.

[65] L. Löfler, R. Hahn, P.H. Mayrhofer, M. Bartosik, D. Holec, Mechanical properties of CrN-based superlattices: impact of magnetism, Acta Mater. 218 (2021) 117095, doi:10.1016/j.actamat.2021.117095.

[66] D. Holec, L. Zhou, H. Riedl, C.M. Koller, P.H. Mayrhofer, M. Friák, M. Šob, F. Körmann, J. Neugebauer, D. Music, M.A. Hartmann, F.D. Fischer, Atomistic modeling-based design of novel materials, Adv. Eng. Mater. 19 (2017) 1–19, doi:10.1002/adem.201600688.

[67] D. Holec, P.H. Mayrhofer, Surface energies of AlN allotropes from first principles, Scr. Mater. 67 (2012) 760–762, doi:10.1016/j.scriptamat.2012.07.027.

[68] N. Koutná, P. Řehák, Z. Chen, M. Bartosik, M. Fallmann, M. Černý, Z. Zhang, M. Friák, M. Šob, P.H. Mayrhofer, D. Holec, Correlating structural and mechanical properties of AlN/TiN superlattice films, Scr. Mater. 165 (2019) 159–163, doi:10.1016/j.scriptamat.2019.02.021.

[69] D. Holec, M. Friák, J. Neugebauer, P.H. Mayrhofer, Trends in the elastic response of binary early transition metal nitrides, Phys. Rev. B Condens. Matter Mater. Phys. (2012) 85, doi:10.1103/PhysRevB.85.064101.

[70] M. Bartosik, R. Daniel, C. Mitterer, J. Keckes, Thermally-induced formation of hexagonal AlN in AlCrN hard coatings on sapphire: Orientation relationships and residual stresses, Surf. Coat. Technol. 205 (2010) 1320–1323, doi:10.1016/j.surfcoat.2010.08.089.

[71] L. Hultman, Thermal stability of nitride thin films, Vacuum 57 (2000) 1–30, doi:10.1016/s0042-207x(00)00143-3.

[72] M. Tkadletz, C. Hofer, C. Wüstefeld, N. Schalk, M. Motylenko, D. Rafaja, H. Holzschuh, W. Bürgin, B. Sartory, C. Mitterer, C. Czettl, Thermal stability of nanolamellar fcc-$Ti_{1-x}Al_xN$ grown by chemical vapor deposition, Acta Mater. 174 (2019) 195–205, doi:10.1016/j.actamat.2019.05.044.

[73] M. Tkadletz, A. Lechner, N. Schalk, B. Sartory, A. Stark, N. Schell, C. Saringer, C. Mitterer, C. Czettl, Influence of spinodal decomposition and fcc→w phase transformation on global and local mechanical properties of nanolamellar CVD fcc-Ti1-xAlxN coatings, Materialia 11 (2020), doi:10.1016/j.mtla.2020.100696.

[74] F. Cernuschi, P.G. Bison, S. Marinetti, P. Scardi, Thermophysical, mechanical and microstructural characterization of aged free-standing plasma-sprayed zirconia coatings, Acta Mater. 56 (2008) 4477–4488, doi:10.1016/j.actamat.2008.04.067.

[75] H.J. Rätzer-Scheibe, U. Schulz, The effects of heat treatment and gas atmosphere on the thermal conductivity of APS and EB-PVD PYSZ thermal barrier coatings, Surf. Coat. Technol. 201 (2007) 7880–7888, doi:10.1016/j.surfcoat.2007.03.028.

[76] N. Markocsan, P. Nylén, J. Wigren, X.H. Li, A. Tricoire, Effect of thermal aging on microstructure and functional properties of zirconia-base thermal barrier coatings, J. Therm. Spray Technol. 18 (2009) 201–208, doi:10.1007/s11666-009-9313-6.

[77] G. Mehboob, M.J. Liu, T. Xu, S. Hussain, G. Mehboob, A. Tahir, A review on failure mechanism of thermal barrier coatings and strategies to extend their lifetime, Ceram. Int. 46 (2020) 8497–8521, doi:10.1016/j.ceramint.2019.12.200.

[78] P.H. Mayrhofer, A. Hörling, L. Karlsson, J. Sjölén, T. Larsson, C. Mitterer, L. Hultman, Self-organized nanostructures in the Ti-Al-N system, Appl. Phys. Lett. 83 (2003) 2049–2051, doi:10.1063/1.1608464.

[79] R. Franz, M. Lechthaler, C. Polzer, C. Mitterer, Oxidation behaviour and tribological properties of arc-evaporated ZrAlN hard coatings, Surf. Coat. Technol. 206 (2012) 2337–2345, doi:10.1016/j.surfcoat.2011.10.023.

[80] P.H. Mayrhofer, H. Willmann, A.E. Reiter, Structure and phase evolution of Cr-Al-N coatings during annealing, Surf. Coat. Technol. 202 (2008) 4935–4938, doi:10.1016/j.surfcoat.2008.04.075.

[81] C. Sabitzer, J. Paulitsch, S. Kolozsvári, R. Rachbauer, P.H. Mayrhofer, Impact of bias potential and layer arrangement on thermal stability of arc evaporated Al-Cr-N coatings, Thin Solid Films 610 (2016) 26–34, doi:10.1016/j.tsf.2016.05.011.

[82] F. Medjani, R. Sanjinés, G. Allidi, A. Karimi, Effect of substrate temperature and bias voltage on the crystallite orientation in RF magnetron sputtered AlN thin films, Thin Solid Films 515 (2006) 260–265, doi:10.1016/j.tsf.2005.12.145.

[83] H.C. Lee, J.Y. Lee, H.J. Ahn, Effect of the substrate bias voltage on the crystallographic orientation of reactively sputtered AlN thin films, Thin Solid Films 251 (1994) 136–140, doi:10.1016/0040-6090(94)90678-5.

[84] R. Daniel, M. Meindlhumer, W. Baumegger, J. Todt, J. Zalesak, T. Ziegelwanger, C. Mitterer, J. Keckes, Anisotropy of fracture toughness in nanostructured ceramics controlled by grain boundary design, Mater. Des. 161 (2019) 80–85, doi:10.1016/j.matdes.2018.11.028.

[85] O. Kolednik, J. Predan, F.D. Fischer, P. Fratzl, Bioinspired design criteria for damage-resistant materials with periodically varying microstructure, Adv. Funct. Mater. 21 (2011) 3634–3641, doi:10.1002/adfm.201100443.

[86] M. Sistaninia, O. Kolednik, A novel approach for determining the stress intensity factor for cracks in multilayered cantilevers, Eng. Fract. Mech. 266 (2022) 108386, doi:10.1016/j.engfracmech.2022.108386.

[87] M. Kuzmina, D. Ponge, D. Raabe, Grain boundary segregation engineering and austenite reversion turn embrittlement into toughness: example of a 9 wt.% medium Mn steel, Acta Mater. 86 (2015) 182–192, doi:10.1016/j.actamat.2014.12.021.

[88] M. Herbig, M. Kuzmina, C. Haase, R.K.W. Marceau, I. Gutierrez-Urrutia, D. Haley, D.A. Molodov, P. Choi, D. Raabe, Grain boundary segregation in Fe-Mn-C twinning-induced plasticity steels studied by correlative electron backscatter diffraction and atom probe tomography, Acta Mater. 83 (2015) 37–47, doi:10.1016/j.actamat.2014.09.041.

[89] H. Zhao, F. De Geuser, A. Kwiatkowski da Silva, A. Szczepaniak, B. Gault, D. Ponge, D. Raabe, Segregation assisted grain boundary precipitation in a model Al-Zn-Mg-Cu alloy, Acta Mater. 156 (2018) 318–329, doi:10.1016/j.actamat.2018.07.003.

[90] J. Buchinger, A. Wagner, Z. Chen, Z.L. Zhang, D. Holec, P.H. Mayrhofer, M. Bartosik, Fracture toughness trends of modulus-matched TiN/(Cr,Al)N thin film superlattices, Acta Mater. 202 (2021) 376–386, doi:10.1016/j.actamat.2020.10.068.
[91] T. Glechner, R. Hahn, T. Wojcik, D. Holec, S. Kolozsvári, H. Zaid, S. Kodambaka, P.H. Mayrhofer, H. Riedl, Assessment of ductile character in superhard Ta-C-N thin films, Acta Mater. 179 (2019) 17–25, doi:10.1016/j.actamat.2019.08.015.
[92] T. Glechner, S. Lang, R. Hahn, M. Alfreider, V. Moraes, D. Primetzhofer, J. Ramm, S. Kolozsvári, D. Kiener, H. Riedl, Correlation between fracture characteristics and valence electron concentration of sputtered Hf-C-N based thin films, Surf. Coat. Technol. 399 (2020) 126212, doi:10.1016/j.surfcoat.2020.126212.
[93] X. Liu, C.E. Athanasiou, N.P. Padture, B.W. Sheldon, H. Gao, A machine learning approach to fracture mechanics problems, Acta Mater. 190 (2020) 105–112, doi:10.1016/j.actamat.2020.03.016.
[94] X. Liu, C.E. Athanasiou, N.P. Padture, B.W. Sheldon, H. Gao, Knowledge extraction and transfer in data-driven fracture mechanics, Proc. Natl. Acad. Sci. U.S.A. 118 (2021), doi:10.1073/pnas.2104765118.